

The Diffuse and Compact X-ray Components of the Starburst Galaxy Henize 2-10

Henry A. Kobulnicky

*Department of Physics & Astronomy
University of Wyoming
Laramie, WY 82070*

chipk@uwyo.edu

Crystal L. Martin

*University of California, Santa Barbara
Department of Physics
Santa Barbara, CA 93106*

cmartin@physics.ucsb.edu

ABSTRACT

Chandra X-ray Observatory imaging spectroscopy of the starburst galaxy Henize 2-10 reveals a strong nuclear point source and at least two fainter compact sources embedded within a more luminous diffuse thermal component. Spectral fits to the nuclear X-ray source imply an unabsorbed X-ray luminosity $L_x > 10^{40}$ erg s⁻¹ for reasonable power law or blackbody models, consistent with accretion onto a $>50 M_\odot$ black hole behind a foreground absorbing column of $N_H > 10^{23}$ cm⁻². Two of these point sources have $L_x = 2 - 5 \times 10^{38}$ erg s⁻¹, comparable to luminous X-ray binaries. These compact sources constitute a small fraction ($\leq 16\%$) of the total X-ray flux from He 2-10 in the 0.3–6.0 keV band and just 31% of the X-rays in the hard 1.1–6.0 keV band which is dominated by diffuse emission. Two-temperature solar-composition plasmas ($kT \simeq 0.2$ keV and $kT \simeq 0.7$ keV) fit the diffuse X-ray component as well as single-temperature plasmas with enhanced α/Fe ratios. Since the observed radial gradient of the X-ray surface brightness closely follows that of the H α emission, the composition of the X-ray plasma likely reflects mixing of the ambient cool/warm ISM with an even hotter, low emission measure plasma, thereby explaining the \sim solar ISM composition. Aperture synthesis 21-cm maps show an extended neutral medium to radii of 60'' so that the warm and hot phases of the ISM, which extend to $\sim 30''$, are enveloped within the 8×10^{20} cm⁻² contour of the cool neutral medium. This

extended neutral halo may serve to inhibit a starburst-driven outflow unless it is predominantly along the line of sight. The high areal density of star formation can also be reconciled with the lack of prominent outflow signatures if Henize 2-10 is in the very early stages of developing a galactic wind.

Subject headings: galaxies: formation — galaxies: evolution — galaxies: fundamental parameters — galaxies: abundances

1. Introduction

1.1. Goals of this Study

The blue compact galaxy Henize 2-10 has been extensively studied as the prototype of starbursting galaxies containing large populations of Wolf-Rayet stars (Conti 1991). As a galaxy hosting recent intense star formation activity, He 2-10 is a natural target for investigating the impact of starbursts on interstellar medium. In Henize 2-10, supernova activity has apparently produced a hot X-ray emitting component and has arguably impacted the composition and kinematics of the warm and cold ISM components as well (Méndez et al. 1999; Johnson et al. 2000; Ott et al. 2005; Grimes et al. 2005; Schwartz et al. 2006). Our goal in this paper is to provide a systematic overview of the physical state of and the relation between these components using a panchromatic suite of X-ray, optical, and radio datasets. We use a 20 ksec imaging observation with the *Chandra X-ray Observatory* in order to characterize the distribution of the hot X-ray emitting plasma in relation to the ionized and neutral gas and provide a complete analysis of the X-ray point source population in and around He 2-10. Previous analyses of these *Chandra* data by Ott et al. (2005) and Grimes et al. (2005) have addressed the integrated X-ray properties of He 2-10 in the context of larger samples of star-forming galaxies with diffuse X-ray emission. These studies concluded that the hot ISM is mildly enriched in α -process elements, consistent with the mixing of fresh supernova ejecta from the recent starburst into the surrounding ISM. Our focus here is a more detailed look at both the diffuse and compact X-ray components of He 2-10 than previously reported. We show that α -element enrichment is not strictly required to fit the X-ray spectrum, we identify a hard ultraluminous X-ray source as a counterpart to a nuclear radio source, and we discuss the relative energetics and morphologies of the cold, warm, and hot phases of the ISM to understand the state of the starburst-driven outflow. First, we provide a brief review of the global characteristics of He 2-10 that will be relevant to later discussion.

1.2. Henize 2-10: Content and Kinematics

Morphological studies reveal at least three distinct starforming regions as shown in the images of Méndez et al. (1999). The most luminous central starburst region contains 6–10 compact ($<1''$) super starclusters which have diameters of <10 pc at the nominal 9.8 Mpc distance of He 2-10.¹ These clusters have ages <10 Myr and masses up to $10^5 M_{\odot}$ (Conti & Vacca 1994; Johnson et al. 2000; Vacca et al. 2002). Chandar et al. (2003) assign an age range of 4–5 Myr for the four most luminous clusters.

Radio interferometer observations reveal the presence of at least four radio-bright “ultra-dense” H II regions powered by very young super starclusters (Kobulnicky & Johnson 1999; Johnson & Kobulnicky 2003). The $H\alpha$ luminosity of Henize 2-10 (not corrected for extinction) measured by Méndez et al. (1999) is 2.1×10^{41} erg s⁻¹, leading to an implied current star formation rate of $>1.8 M_{\odot}$ yr⁻¹ based on the formulation of Kennicutt (1989). Given the relatively small $20'' \times 20''$ (0.89 kpc²) region containing all of this activity, the star formation rate per unit area is at least $\simeq 2 M_{\odot}$ yr⁻¹ kpc⁻². The *Spitzer Space Telescope* 24 μ m flux of 4.9 Jy (Engelbracht et al. 2005) implies a much higher star formation rate of $6.8 M_{\odot}$ yr⁻¹ using the calibration of Calzetti et al. (2007), indicating that much of the star formation is heavily obscured (Vacca et al. 2002).

He 2-10 contains an H I mass of $4.9 \times 10^8 M_{\odot}$ (Kobulnicky et al. 1995) and molecular mass of $2.9 \times 10^8 M_{\odot}$ yielding a helium-corrected gas mass fraction of ≤ 0.20 , consistent with Henize 2-10 being a transition object between gas-rich dwarfs and larger, more gas-poor spiral galaxies. Beam-averaged H I column densities in the central region vary from few $\times 10^{20}$ cm⁻² to as high as 2×10^{22} cm⁻² (Baas et al. 1994; Kobulnicky et al. 1995; Meier et al. 2001; Santangelo et al. 2009) corresponding to extinctions up to $A_V=20$ mag for typical Galactic gas-to-dust ratios (Bohlin et al. 1978). This is consistent with the localized high extinctions of $A_V=10$ –30 mag inferred from mid-IR silicate absorption and IR Brackett emission-line methods (Phillips et al. 1984; Kawara et al. 1989; Beck et al. 1997) but much higher than the $A_V=1$ –2 mag derived toward optically visible star clusters and H II regions (Vacca & Conti 1992). These disparate results warn that the nuclear conditions are complex on small angular scales with large variations along the line of sight. This high dust and molecular content is consistent with the strong CO emission and with chem-

¹The observed optical and 21-cm radial velocities (Kobulnicky et al. 1995; Méndez et al. 1999; Schwartz 2005) corrected for Galactic rotation and Virgocentric infall yield a Hubble-flow velocity of ~ 712 km s⁻¹, leading to a distance of 9.8 Mpc for $H_0 = 72$ km s⁻¹ Mpc⁻¹. This implies an angular scale of 47 pc arcsec⁻¹ and a distance modulus of 29.95 mag. Throughout, we convert linear distances and implied luminosities from prior works self-consistently to this distance. Distances ranging from 9 to 14 Mpc may be found in the literature.

ical abundance measurements showing a metallicity near the solar value (Kobulnicky et al. 1999). Darling et al. (2008) detect H₂O “kilomasers” in the nucleus, indicating the presence of many massive star-forming regions. Single-dish radio continuum measurements over a range of frequencies show a dominant non-thermal component, indicating the presence of significant supernova activity (Allen et al. 1976). H α images of Henize 2-10 show multiple ionized shells and filaments typical of actively starforming dwarf galaxies (Marlowe et al. 1995). High-resolution H α spectroscopy reveals multiple kinematic components, with the fastest reaching $\Delta V = 250 \text{ km s}^{-1}$ (Méndez et al. 1999).

Blueshifted interstellar absorption lines seen against the nucleus indicate an outflow of low-ionization material along the line of sight (Schwartz et al. 2006; Johnson et al. 2000). Published outflow speeds vary by a factor of two owing to uncertainties regarding the systemic velocity, low spectral resolution, and the wavelength ambiguity caused by the uncertain positioning of the continuum source within a large spectral aperture. Optical echelle spectroscopy obtained with HIRES at the W. M. Keck Observatory offer the most accurate measurements to date (Schwartz 2005). Excited stellar Mg I triplet $\lambda\lambda$ 5167.32, 5172.68, 5183.60 Å absorption yields a heliocentric systemic velocity of $869 \pm 3 \text{ km s}^{-1}$, consistent with the 21-cm and CO data. The narrow slit and seven km s^{-1} resolution reveal four blueshifted interstellar Na I $\lambda\lambda$ 5889.95, 5895.92 Å components in addition to a stellar absorption component at the systemic velocity. The fastest (and weakest) of these reaches a maximum velocity of -180 km s^{-1} . The average outflow speeds of the four components are -34 ± 2 , -65 ± 2 , -93 ± 4 , and $-128 \pm 2 \text{ km s}^{-1}$.

The maximum H I rotation velocity observed by Kobulnicky et al. (1995) provides a lower limit on the dynamical mass of He 2-10. For the adopted distance of 9.8 Mpc and an inclination of 30 degrees, the dynamical mass within 2.1 kpc is $M_{dyn} = 1.18 \times 10^{10} M_{\odot}$. The modified isothermal sphere model of Ferrara & Tolstoy (2000) for the mass distribution implies a halo scale radius of 4.8 kpc and a central density of $9.5 \times 10^6 M_{\odot} \text{ kpc}^3$. We estimate the escape velocity at the disk radius of 2.1 kpc is at least 150 km s^{-1} for a disk inclination of 30 degrees. Hence little of the observed outflow exceeds the escape velocity. A decrease in the covering fraction of the low-ionization gas with radius (Martin & Bouché 2009) and/or increasing ionization fraction with radius, however, might render higher velocity gas difficult to detect.

2. Data Acquisition and Reduction

2.1. *Chandra* Observations

The *Chandra X-ray Observatory* observed Henize 2-10 with the *Chandra* CCD Imaging Spectrometer (ACIS) on 2001 March 23 for 20.02 ksec. The galaxy was placed on the back-illuminated chip ACIS-S3 (also known as chip 7). These data, as well as the fields on the ACIS-I and ACIS-S5 chips, are available in the archive under sequence number 600209.

The data were processed by the *Chandra* X-ray Center (CXC) using version R4CU5UPD14.1 of their software. CIAO, version 2.3, with CALDB, version 2.4, was used for the majority of the data processing unless otherwise noted. We checked the positional accuracy of the chip 7 *Chandra* sources using our R-band image. For the 9 X-ray sources with optical detections, the rms positional discrepancy was found to be $0''.5$. The light curve was inspected, and no periods of high background occurred during the observation. No additional re-processing was required.

Spectra were extracted using pulse invariant data values to account for gain variations between nodes. For each source region, we weighted the appropriate CXC spectral response files by the distribution of their areas within the aperture.² The maximum difference between our area-weighted response files and single response files extracted at the flux-weighted centroid of the aperture was a few percent. Weighting the response files by the distribution of counts within the aperture produced results indistinguishable from the area-weighted responses.

Unbinned images were extracted from the time-filtered events file in four carefully chosen bands: soft (S) 0.3–0.7 keV, medium (M) 0.7–1.1 keV, hard (H) 1.1–6 keV, and Total (T) 0.3–6 keV. Emission in the soft band is somewhat attenuated because the Galactic foreground column, $N_H = 4.89 \times 10^{20} \text{cm}^{-2}$ (Hartmann & Burton 1996), corresponds to optical depth unity at 0.35 keV. The galaxy was not detected at energies above 6 keV, the energy adopted for the hard band cutoff. Background images were extracted from the background events file in these bands.

Each of the four X-ray images was smoothed using the adaptive smoothing algorithm of H. Ebeling & V. Rangarajan as implemented as CSMOOTH in CIAO. The smoothing scales are automatically adjusted to achieve a minimum S/N ratio of 1.8 and a maximum S/N ratio of 2.2 per pixel. Strong point sources are effectively unchanged by the smoothing

²We used the `calcrmf/calcarf` software package contributed by Jonathon McDowell which is available from the CXC website – <http://asc.harvard.edu/cgi-gen/cont-soft/soft-list.cgi>.

process, while the contrast of weak, diffuse emission is enhanced. Each of the four background images was smoothed (using the smoothing map generated by CSMOOTH from the on-source images) and subtracted from the source images.

Since adaptive smoothing does not preserve photon statistics in a straightforward manner, we used the adaptively smoothed images only to produce images for presentation and to define large apertures for the extraction of diffuse component spectra. All quantitative analyses were performed by extracting photons from the events file or unsmoothed images and by estimating their significance using Poisson statistics.

2.2. Point Source Identification

The CIAO 4.1 detection algorithms CELLDETECT and WAVDETECT were used to identify compact X-ray sources on the ACIS S3 chip over the energy range 0.3 – 6 keV. We used WAVDETECT with wavelet scales between 1 and 32 pixels as the primary detection tool, and this yielded 29 probable X-ray sources, the weakest of which had a significance level of 1.7σ . Three sources (#’s 1,2,3) lie projected against the stellar component of He 2-10, while the remainder may be associated with field stars or background galaxies. CELLDETECT found a subset of these 29 sources, but also yielded four additional sources not identified by WAVDETECT (#’s 30 – 33). These four lie within $10''$ of the nucleus where the diffuse X-ray emission is strong, have sizes exceeding the nominal PSF size, and, we show later, are likely to be localized peaks in the diffuse thermal emission. Table 1 lists the positions of the 29+4 compact sources detected. Figure 1 shows these sources numbered 1–29 overlaid on an optical 6550 Å image. Sources 1,2,3 and 30–33 are better seen in Figure 2 which shows an adaptively smoothed X-ray depiction (*contours*) of the Henize 2-10 nucleus overlaid on a 400 s F814W image (*grayscale*) from the Hubble Space Telescope archive (Johnson et al. 2000). Figure 3 shows an unsmoothed 0.3 – 6 keV X-ray image of the ACIS S3 chip with the elliptical source regions, as in Figure 1. The inset in this Figure shows a zoomed view near the nucleus that includes sources 1,2,3 and 30–33.

We measured counts in each of the four energy bands (Total, Soft, Medium, and Hard) using elliptical apertures containing probable source pixels as identified by WAVDETECT. Annuli surrounding each aperture were defined manually and used for measuring and subtracting the background. Table 1 lists the net counts detected in each band along with the ratio of the source size to the nominal PSF. Sources 1,2,3, 10 and 30–33 have PSF ratios near 2 or larger, suggesting that they may be either extended sources or blends of multiple point sources.

Our detection threshold of ~ 4 counts in 20 ksec in the Total 0.3–6 keV band on the *Chandra ACIS* corresponds to an X-ray flux of 1.5×10^{-15} based on the WebPIMMS mission count rate simulator. At or above this flux level we would expect an X-ray source density of ~ 0.8 sources per square arcminute, based on the results of Mushotzky et al. (2000), Moretti et al. (2003), and Kim et al. (2007). Within the ~ 0.25 square degree region encompassing He 2-10, we would therefore expect, on average, 0.2 background X-ray sources. Statistically, the three (possibly seven) compact sources projected onto He 2-10 are likely to lie within the galaxy itself.

2.3. Optical imaging

Optical images of He 2-10 were obtained the night of 2001 March 28 with the 3.5 m WIYN³ telescope and the MiniMosaic detector. Seeing was highly variable, and non-photometric conditions prevailed. Exposures of 60 s were obtained using a filter of width 385 Å centered at 6550 Å. Two exposures with the smallest point spread functions were combined to produce an image with a mean stellar FWHM of 1.2". A rough R-band flux calibration was performed on the image using the magnitudes of 8 stars in the field based on the Guide Star Catalog F-band magnitudes. The typical uncertainty is 0.5 mag. Poor weather and low target elevation prevented $H\alpha$ narrow band exposures from being taken. We instead obtained a continuum-subtracted $H\alpha$ image of Henize 2-10 which appeared in Méndez et al. (1999) (kindly given to us by C. Esteban.) The $H\alpha$ image is flux calibrated using the calibration of Méndez et al. (1999).

2.4. Radio Continuum Observations

Radio continuum observations of Henize 2-10 at 20 cm (1420 MHz) and 2 cm (15 GHz) were obtained with the Very Large Array in the B configuration and published previously in Koblunicky et al. (1995) and Koblunicky & Johnson (1999). Full details may be found in those papers. We used the 20-cm data mapped with a synthesized beam of 3" FWHM to search for radio sources in the field surrounding He 2-10 that correspond to the detected X-ray and optical sources. Other than Henize 2-10 itself, there are no 20-cm radio sources within the 8' *Chandra* field to a 3σ limit of 0.6 mJy.

³The WIYN Observatory is a joint facility of the University of Wisconsin-Madison, Indiana University, Yale University, and the National Optical Astronomy Observatory.

3. X-ray Properties

3.1. Nature of the Point Sources

Sources 1–3 and 30–33 appear superimposed on diffuse emission near the nucleus of Henize 2-10, and all have PSF ratios between 2 and 4, while the remainder of the 26 compact sources further from the nucleus have PSF ratios not far from unity. These nuclear objects may either be genuine point sources (i.e., X-ray binaries or collections of X-ray binaries) projected onto regions of diffuse gas, or they may be local maxima in the diffuse emission. The second possibility better explains their larger sizes compared to the field sources. Their X-ray colors help to discriminate between these possibilities.

Figure 4 shows an X-ray two-color diagram formed from ratios of count rates in the hard, medium, and soft bandpasses: $(M - S)/(M + S)$ and $(H - M)/(H + M)$. The left panels include only the seven sources projected against the nucleus, while right panels show the other 26 sources. Lines and filled circles illustrate the X-ray colors for various power law, thermal plasma (MEKAL), and blackbody spectral energy distributions for four different foreground absorbing columns: 0.0, 0.2×10^{22} , 0.8×10^{22} , and 1.6×10^{22} cm⁻². Sources 1–3 are consistent with $\Gamma = 1.5$ power law spectra behind modest absorbing columns. These three objects are strongest in the hard band, consistent with heavily absorbed spectra. Sources 2 and 3 are too faint for meaningful spectral fits, but lower limits on their luminosities can be made assuming a *minimum* column density of $N_H = 0.05 \times 10^{22}$ cm⁻² for the Galactic foreground and a power law spectrum with photon index $\Gamma = 1$ where the number of photons per energy bin is given by $N(E) \propto E^{-\Gamma}$. For these values, sources 2 and 3 have probable unabsorbed 0.3–8 keV luminosities of $>3.4 \times 10^{38}$ erg s⁻¹ and $>1.7 \times 10^{38}$ erg s⁻¹ respectively at 9.8 Mpc. Although not quite as luminous as the “superluminous” X-ray sources found in nearby galaxies ($> 10^{39}$ erg s⁻¹; e.g., Roberts et al. (2004)), these objects are likely to be powered by accretion onto stellar mass black holes. However, the uncertainties in the foreground column and the photon energy distribution would allow for intrinsic luminosities several times greater than these estimates if N_H and Γ were larger than the values adopted here. We note that both of these objects appear to lie within the older starburst region “B” (Vacca & Conti 1992) several arcseconds to the east of the dominant starburst core region (“A”).

By contrast with sources 2 & 3, sources 30–33 are strongest in the medium band, consistent with the color expected of soft thermal plasma. The upper right panel of Figure 4 plots the colors of sources 4–29. We tentatively identify these sources as either stars or active galactic nuclei (AGN) based on the ratio of their X-ray to optical fluxes, following Krautter et al. (1999). The ratio of X-ray to optical fluxes is f_X/f_V , where f_X (erg s⁻¹ cm⁻²)

$= 3.6 \times 10^{-16} \times C_{tot}$ where C_{tot} is the number of detected 0.3–6.0 keV X-ray photons in 20 ks, and $f_V(\text{erg s}^{-1} \text{ cm}^{-2}) = 1.7 \times 10^{-6} \times 2.5^{-R}$ where R is the R-band magnitude. Table 1 lists objects with $\log(f_X/f_V) < -0.5$ as probable stars and objects with $\log(f_X/f_V) > -0.5$ as probable AGN. In Figure 4, probable stars appear as filled squares and probable AGN appear as crosses. Solid dots connected by lines indicate the colors of MEKAL thermal plasmas with temperatures of 0.5, 1.0, and 2.0 keV attenuated by absorbing columns of 0.0, 0.2×10^{22} , 0.4×10^{22} , 0.8×10^{22} , and $1.6 \times 10^{22} \text{ cm}^{-2}$. The candidate stars occupy a region of relatively low column density, as might be expected for Galactic foreground objects. The candidate AGN are distributed throughout the diagram, consistent with a range of power law slopes and absorbing columns. The strongest source in the field is object 7, the star GSC 06578-03010. It is a previously known X-ray source, RX J0836.0-2621.

3.2. Diffuse versus Point Source Flux Contributions

The compact sources 1–3 represent only a small fraction of the X-ray flux of Henize 2-10. We performed photometry on the X-ray images using an $80''$ diameter aperture centered on the nucleus to obtain a total flux for the galaxy. The size of this aperture was chosen to include all of the diffuse emission seen in the smoothed, background-subtracted total band (0.3–6.0 keV) image. This aperture includes the seven compact sources in the main body of Henize 2-10 and none of the other 26 sources in the field. The background flux was estimated using an annular region extending $15''$ beyond the circular aperture. Table 2 lists the results of this photometry in each band. Table 2 also indicates the fraction of diffuse emission after subtraction of the flux from the compact sources 1–3. We find that $84 \pm 4\%$ of the emission in the total 0.3–6.0 keV band comes from diffuse emission. In the hard 1.1–6.0 keV band, $69 \pm 9\%$ of the emission is diffuse. In the soft and medium bands, the fraction of flux from the diffuse X-ray medium is over 90%. Thus, the X-ray flux of Henize 2-10 appears to be dominated by the diffuse plasma component even in the highest energy band.

3.3. X-ray Spectrum of the Nuclear Source: An Intermediate-Mass Black Hole?

Johnson & Koblunicky (2003) noted the non-thermal nature of the spectral energy distribution of the pointlike radio source in the nucleus (source #3 of Koblunicky & Johnson (1999)) but did not discuss the nature of this source. Figure 5 shows the X-ray contour image from Figure 2 overlaid on a grayscale representation of the 2 cm (15 GHz) radio map from Koblunicky & Johnson (1999). Radio source KJ3, marked by a star, lies $0.25''$ south of the

brightest nuclear X-ray source, #1. Within the uncertainties of the radio and X-ray data, the two sources are coincident. The optical and mid-IR images of Cabanac et al. (2005) show that there is no bright optical or infrared source at this location.⁴

We extracted an X-ray spectrum of the region within $1''$ (~ 2 pix) of the dominant X-ray source, #1, using a neighboring annular region to estimate the local X-ray background. Other choices of local background yield similar results. The resulting spectrum, shown in Figure 6, was then analyzed in Xspec (version 11.3). No single-component spectral models produce acceptable fits to the data. Reasonable models require at least two spectral components to reproduce both the low-energy peak near 1 keV and the secondary peak near 3 keV. This secondary high-energy peak is most pronounced in small $2''$ diameter spectral apertures centered on the nucleus and becomes weaker relative to the rest of the spectrum as the aperture size is increased. This indicates that the high energy photons near 3 keV are concentrated near the nucleus, comprising a real spectral feature of the nuclear source. The observed 0.3–6.0 keV flux from the nuclear source is 7.6×10^{-14} erg s⁻¹ cm⁻². Given the high optical extinction toward the nucleus of Henize 2-10 ($A_V=10$ –30 mag; Phillips et al. (1984); Kawara et al. (1989)) X-rays are likely to provide the best estimate of the bolometric luminosity of the central source.

We performed spectral fits to the nuclear source assuming a minimum foreground Galactic column of 0.05×10^{22} cm⁻² of solar abundance (component WABS⁵ in Xspec). We fit the X-ray SED with spectral models that were linear combinations of a solar-abundance thermal plasma component (MEKAL with variable foreground, N_H , and variable temperature, kT) superimposed on either a power law component (POW with variable N_H and photon index, Γ) or a second thermal component (variable N_H and variable kT). In all cases, the second component required very high foreground columns of more than 2×10^{22} cm⁻² in order that it contribute at 3 keV but not at lower energies. Such high column densities are consistent with the beam-averaged molecular gas column densities toward the nucleus (Kobulnicky et al. 1995) and correspond to optical extinctions of $A_V=20$ for typical Galactic ratios $N_{H_2}/A_V = 9.4 \times 10^{20}$ cm⁻² mag⁻¹ (Bohlin et al. 1978).

The best fitting models have reduced $\chi^2 \simeq 1$ and involve an absorbed MEKAL ther-

⁴Cabanac et al. (2005) identify and correct erroneous astrometry in the *HST* images that were used to compare optical and radio/IR positions in Kobulnicky & Johnson (1999), Vacca et al. (2002), Johnson & Kobulnicky (2003), and in some earlier works. The net result is that the *HST* images should be shifted $1''.2$ west relative to the radio and IR images in Figures from those prior publications.

⁵Adopting a model for the absorbing ISM based on the more recent X-ray cross sections of Wilms et al. (2000) (TABS in Xspec) changes the best fit parameters negligibly.

mal plasma component and a heavily absorbed power law component (WABS(MEKAL + WABS*POW)). Table 3 summarizes the parameters, χ^2 values, and implied unabsorbed luminosities for a range of power law photon index, Γ , ranging from 1 to 4. In these fits the temperature of the thermal component is fixed at 0.4 keV, while the normalizations and absorbing columns of each component are allowed to vary. Model A which has a steep power law index of $\Gamma = 4$ and very high absorbing column of $24 \times 10^{22} \text{ cm}^{-2}$ produces the best fit, having reduced $\chi^2=0.89$ for 9 degrees of freedom. Such a steep power law index is consistent with the class of “super soft” extragalactic X-ray sources (Cagnoni et al. 2003) and some of the ultraluminous X-ray sources in the compilations of Winter et al. (2006) and Berghea et al. (2008). Models B and C with $\Gamma = 2$ and $\Gamma = 1$, respectively, also yield acceptable fits with $\chi^2=1.10$ and $\chi^2=1.33$. Substituting a 500–700 eV blackbody component for the power law component produces similar acceptable fits. In general, steeper power law photon indices require larger absorbing column densities. In this series of models, the normalization of the power law component ranges from a factor of 10 to a factor of two larger than the MEKAL component, indicating that the power law component dominates the SED. Neither the slope of the photon index, Γ , nor the foreground column density are well constrained given that there are only 142 total counts in the X-ray spectrum. However, the best fit parameters represent reasonable physical conditions similar to those observed in studies of X-ray binaries (Remillard & McClintock 2006) and extragalactic X-ray point source populations (Strickland et al. 2000; Zezas & Fabbiano 2002).

Any of the the models in Table 3 imply an *unabsorbed* 0.3–6.0 keV X-ray luminosity in the central $2''$ of $L_{X(0.3-6.0)} \simeq 10 \times 10^{38} \text{ erg s}^{-1}$ to as much as $L_{X(0.3-6.0)} \simeq 1200 \times 10^{38} \text{ erg s}^{-1}$ for a distance of 9.8 Mpc. Such luminosities are similar to the ultraluminous (ULX) X-ray point sources with $L_X = 10^{39} - 10^{41} \text{ erg s}^{-1}$ which are common in nearby galaxies (Colbert & Ptak 2002; Swartz et al. 2004; Winter et al. 2006; Berghea et al. 2008). Some galaxies like the Antennae (NGC 4038/39) harbor several (Zezas & Fabbiano 2002).

The physical nature of ULX sources has not been firmly established. They may be stellar mass black holes accreting at super-Eddington rates or radiating non-isotropically (i.e., beamed) (King et al. 2001; K rding et al. 2002; Rappaport et al. 2005; King 2009), or they may be intermediate-mass black holes with $M=20\text{--}10000 M_\odot$ (Colbert & Mushotsky 1999; Miller & Colbert 2004). Some combination of these possibilities is likely. ULX sources are usually associated with regions of star formation, often have optical counterparts (Ramsey et al. 2006), and are uncommon (Irwin et al. 2004) but not non-existent (Ptak et al. 2006) in early-type galaxies.

If we adopt an X-ray luminosity of $\sim 1 \times 10^{40} \text{ erg s}^{-1}$ for the isotropic luminosity of an accreting object in Henize 2-10, then the implied mass of the central object is $M \geq 100$

M_{\odot} , where the inequality covers the possibility that the object may accrete at rates below the Eddington rate. The formulation of Merloni et al. (2002) expressing the black hole mass in terms of the X-ray and radio luminosity gives $46 M_{\odot}$. This mass is much less than the predicted mass of a nuclear black hole, $M = few \times 10^5 M_{\odot}$, obtained by using the H I velocity dispersion of $\sigma_v = 46 \text{ km s}^{-1}$ (Kobulnicky et al. 1995) with the well-established black hole mass-velocity dispersion correlation (Gebhardt et al. 2000; Tremaine et al. 2002). If the nuclear X-ray source marks the presence of a black hole near the center of Henize 2-10, either the accretion rate is well below the Eddington rate, or the canonical $M_{BH} - \sigma$ relation may not obtain for such a low-mass galaxy.

We extracted time-binned count rates for the central source over the full 0.3–6 keV energy range using bin widths of 2000 s and 4000 s to search for variability. Figure 7 shows the light curve of the nuclear source #1 compared to three other field X-ray sources (#7, #9, #19) with sufficiently high count rates to construct a comparison light curve. Plotted uncertainties reflect photon statistics in the source and background regions. None of the sources show variability at greater than the $1-2\sigma$ level over the 20 ksec period of observation. The nuclear source varies by 40% (2σ), making the evidence for variability marginal.

Another indication of the source nature is the emission at radio wavelengths. Miller et al. (2005) and Lang et al. (2007) report Very Large Array centimeter-wave radio studies of ULX sources in Holmberg II and NGC 5408, respectively, and show that the radio emission is extended over scales of 35–60 pc and has non-thermal spectral indices $\alpha = -0.5 - -0.8$ ($S_{\nu} \propto \nu^{\alpha}$) characteristic of optically thin synchrotron emission in both cases. Such extended emission implies a large ionized nebula. Radio source #3 in He 2-10 (Johnson & Kobulnicky 2003) is also non-thermal ($\alpha \sim -0.9 \pm 0.5$), and, while the angular size is unresolved in the $\sim 1''$ data, implying a diameter smaller than 50 pc, the non-detection of this source with few milliarcsecond resolutions rules out a compact supernova or supernova remnant and suggests an extended morphology (Ulvestad et al. 2007). The ratio of radio to X-ray fluxes for this source, R_X (Terashima & Wilson 2003), is

$$R_X = \frac{\nu L_{\nu}(5 \text{ GHz})}{L_X(2 - 10 \text{ keV})} = \frac{2.9 \times 10^{-16} \text{ erg s}^{-1} \text{ cm}^{-2}}{1.7 \times 10^{-13} \text{ erg s}^{-1} \text{ cm}^{-2}} = 1.7 \times 10^{-3}. \quad (1)$$

This is in the range of other ULX sources and low-luminosity AGN tabulated by Neff et al. (2003) ($R_X = 1 \times 10^{-2} - 2 \times 10^{-3}$), but higher than X-ray transients ($R_X < 10^{-5}$) and lower than a supernova remnant like Cas A ($R_X = 2 \times 10^{-2}$).

3.4. Extended X-ray Emission

Figure 8 show a composite *Chandra* X-ray image of Henize 2-10. Red represents the soft band 0.3–0.7 keV emission, green represents the medium band 0.7–1.1 keV, and blue represents the hard band 1.1–6.0 keV emission. The two probable X-ray binaries to the east of the nucleus (sources 2 and 3) appear blue. The central few arcseconds of the nucleus have the highest surface brightness and appear white, denoting a contribution of X-ray emission in all bands. To the north of the nucleus lies a cone-shaped region with a low X-ray surface brightness, rimmed on both sides by green emission. Several arcseconds to the west of the nucleus lies a red-colored region indicative of soft diffuse emission with lower foreground extinction. A similar red-dominated region lies to the south of the nucleus.

Figure 9 compares the distribution of the warm ionized medium (grayscale), as traced by $H\alpha$ emission, overlaid with the medium-band 0.7–1.1 keV X-rays (contours). Within the inner $10''$, the X-ray and $H\alpha$ emission is elongated in the NW-SE direction, similar to the distribution of molecular gas (Kobulnicky et al. 1995). At larger radii, the diffuse X-rays and the $H\alpha$ have similar morphologies. Ionized features such as the $H\alpha$ shell to the east of the nucleus appear as enhancements in the X-ray image as well. The overall morphology of the galaxy at large radii is nearly circular, without obvious cones of emission or X-shaped features seen emanating from the disks of starburst galaxies (Strickland et al. 2000).

The surface brightness profiles of the diffuse X-ray emission and $H\alpha$ trace each other closely, as found in large samples of star-forming galaxies (Grimes et al. 2005). Figure 10 compare the azimuthally averaged surface brightness of these two ISM components as a function of radius using $2.5''$ wide annuli centered on the nucleus. The left abscissa shows the $H\alpha$ surface brightness in units of $\text{erg s}^{-1} \text{cm}^{-2} \text{arcsec}^{-2}$ and the right abscissa shows the 0.7–1.1 keV X-rays where we have used the best-fit thermal plasma model (see below) to find that 1 photon s^{-1} corresponds to $3.3 \times 10^{-12} \text{erg s}^{-1} \text{cm}^{-2}$. Except for the nuclear region inside $10''$ where extinction may be a significant factor, these tracers of the warm and hot phases, respectively, exhibit the same radial profile. Inside the $10''$ nuclear region, the X-ray surface brightness drops below the $H\alpha$ by a factor of ~ 2.5 (0.4 dex). This may be understood as a result of differential extinction between $H\alpha$, where a column density of $1.5 \times 10^{22} \text{cm}^{-2}$ corresponds to $\tau \sim 4.6$ ($A_V \sim 10$), and the peak of the thermal X-ray emission at 0.7–1.1 keV where $\tau \geq 5.1$ for the same foreground column.

3.4.1. X-rays Relative to the Neutral ISM

The relative distributions of the warm and hot phases are better pictured in Figure 11 which shows the $H\alpha$ emission in red, the 0.7–1.1 keV medium band X-ray emission in green, and the optical continuum 6550 Å in blue. Contours show the molecular gas as traced by ^{12}CO 1-0 emission observed by the Owens Valley Radio Interferometer mapped at a resolution of 5" (Kobulnicky et al. 1995). Although the kinematics of the atomic and molecular gas are complex, CO velocity-field maps show rotation such that the elongation in the CO integrated intensity contours probably traces a molecular “disk” within the rotational plane of Henize 2-10. The $H\alpha$ shells project to the E-NE and SW, presumably driven by starburst activity in the nucleus, and indicate a direction of expansion perpendicular to the molecular disk.

Figure 12 shows the extent of the $H\alpha$ emission (red), the 0.7–1.1 keV medium band X-ray emission (green), and the optical continuum 6550 Å (blue) relative to the neutral hydrogen 21-cm emission in contours (Kobulnicky et al. 1995). The contours correspond to column densities of $N_{\text{HI}} = 2 \times 10^{20}$, 4×10^{20} , 8×10^{20} , and $16 \times 10^{20} \text{ cm}^{-2}$ averaged over a 30" beam. The higher-resolution 21-cm and CO maps of Kobulnicky et al. (1995) indicate that Henize 2-10 does contain regions of much larger H I column density exceeding $N_{\text{HI}} = 4 \times 10^{22} \text{ cm}^{-2}$ on few arcsecond scales, but such localized peaks in the gas surface density are not visible in this low-resolution map. Although the orientation of Henize 2-10 is uncertain, Figure 12 shows that the full extent of X-ray and $H\alpha$ emission (at least to the surface brightnesses probed in the best existing X-ray and $H\alpha$ observations) is contained within the $N_{\text{HI}} = 8 \times 10^{20} \text{ cm}^{-2}$ contour.

If the H I distribution is approximately spherical, then the starburst-driven bubbles have not penetrated the neutral hydrogen envelope, at least to the level of $8 \times 10^{20} \text{ cm}^{-2}$. In contrast, polar superbubbles would have broken through a thick, low-inclination H I disk. The $H\alpha$ emission and neutral gas absorption kinematics allow that we are seeing an expanding polar bubble approximately face-on, but do not require it. Méndez et al. (1999) remark that the superbubbles to the east and north-east are blueshifted, perhaps forming the approaching side of a polar superbubble. The receding lobe could be largely hidden by extinction aside from a bit of redshifted $H\alpha$ emission to the southwest. If the southwest X-ray lobe were viewed through the disk, the X-ray emission in Figure 7 would appear harder to the southwest than it does towards the northeast. In fact, however, Figure 8 shows that the soft (red) regions are preferentially in the south and west. If the lobes are mainly polar, then the X-ray emission must be coming predominantly from the near side of the outflow. Given the evidence for a recent merger in this galaxy (Kobulnicky et al. 1995) combined with the ambiguity of the neutral and ionized gas velocity fields, we conclude that the geometry of the system defies simple characterization and may be dominated by transient features generated

in the merger and outflow.

3.4.2. Spectral Fits to the Diffuse ISM

We extracted a spectrum of the diffuse emission using an annular aperture centered on the nucleus which excludes the $2''$ region containing the nuclear point source. The aperture has an inner radius of $2''$ and an outer radius of $40''$. A $30''$ square region located $60''$ north of He 2-10 was used to estimate the background. Although the spectrum may contain a contribution from faint unresolved X-ray binaries and the probable X-ray binaries Source 2 and Source 2, that contribution is small compared to the diffuse emission. The diffuse spectrum contains 1040 counts and the spectrum was binned to produce a minimum of 15 counts per energy bin.

The diffuse emission was modeled with simple X-ray thermal plasma models in Xspec V11.3. In all cases we adopted a Galactic foreground column density of $5 \times 10^{20} \text{ cm}^{-2}$ based on the integrated H I profile Leiden/Dwingeloo neutral hydrogen survey in this direction (Hartmann & Burton 1996). Table 4 lists the model description, the best fit parameters for these models, the reduced χ^2 value as a goodness-of-fit statistic, and the implied 0.3–6.0 keV unabsorbed luminosity.

Motivated by results in other starburst galaxies where the data required at least two plasma components with different temperatures (Martin et al. 2002; Strickland et al. 2004; Summers et al. 2004), we fit the spectrum with a two-temperature, solar-abundance model, where each component has the same absorbing column density. X-ray bubbles should contain plasma over a range of temperatures from very hot shocked \sim few keV gas to cooler \sim 0.1 keV material at the interface of the X-ray and neutral medium where instabilities and ablation mix the hot gas with the ambient ISM (Strickland et al. 2000). This model (Model 1 in Table 4) produces a good fit to the data (red. $\chi^2=0.97$) with $kT_1=0.68 \text{ keV}$ and $kT_2=0.19 \text{ keV}$ and $N_H=0.5 \times 10^{22} \text{ cm}^{-2}$. Figure 13 shows the binned data and model spectrum (upper panel) along with residuals from the best-fit model (lower panel). By contrast, a single-temperature, single-component, solar-abundance thermal plasma model (Model 2) produces a poor fit to the data (red. $\chi^2=2.25$) for $kT=0.63 \text{ keV}$ and $N_H=0.23 \times 10^{22} \text{ cm}^{-2}$. Allowing the metallicity to vary in the single component model (Model 3) produced a much better fit (red. $\chi^2=1.15$) for $kT=0.63 \text{ keV}$ and $N_H=0.23 \times 10^{22} \text{ cm}^{-2}$ and $\alpha/H=0.14$ (i.e., $Z \simeq 0.14 Z_\odot$). However, we reject such a low metallicity as unphysical given the near-solar abundance of the warm ionized medium (Kobulnicky et al. 1999). Finally, we note that other starburst galaxies show evidence for enhanced ratios of α to iron-group elements (Martin et al. 2002; Grimes et al. 2005; Ott et al. 2005), so we tried a single-component thermal plasma model where the abundances of α and Fe-peak elements were allowed to vary. The α group elements

(C, O, Ne, Mg, Si, S, Ar, Ca) are tied and allowed to vary independently from the Fe-group elements (N, Al, Fe, Ni for these purposes). This model (Model 4) shows an improved fit (red. $\chi^2=0.95$) over models 2 and 3, having $\alpha/H=0.78$, $\alpha/Fe=2.7$, $kT=0.64$ keV, and $N_H=0.1\times 10^{22}$ cm $^{-2}$. These parameters are in good agreement with the previous analyses by Grimes et al. (2005); Ott et al. (2005). Both Models 1 and 4 provide good fits to the data and are consistent with expectations that 1) α/Fe ratios are enhanced in starburst galaxies, and 2) the hot interstellar medium has a range of temperatures, often parameterized as hot and cool X-ray components. Constraining the absolute metallicity of the hot gas in He 2-10 is not possible with these data because of the degeneracy between metallicity and the normalization (i.e., $\int n_e n_H dV/4\pi D^2$) of the X-ray component.

In an attempt to identify spatial variations in the X-ray spectral properties, we extracted spectra using four fan-shaped apertures centered just outside the nucleus and extending 40'' to the north, south, east, and west, similar to the apertures of Ott et al. (2005). All of these apertures exhibited similar spectral characteristics, with the best fit models showing the same anti-correlation between best fitting plasma temperature and absorbing column density. In general, we found that the highest absorbing column densities are located in the east quadrant, but the limited number of photons in each spectrum precludes statistically significant conclusions regarding spatial variations in the diffuse X-ray medium. On the basis of the color differences in Figure 8, we extracted a spectrum of predominantly red (soft X-ray) regions (small fan-shaped regions N and S of the nucleus) and compared the best fit parameters to those for a spectrum of the predominately green (harder X-ray) regions. Once again, the small number of photons, particularly in the red regions of softest X-ray emission, do not constrain the physical properties of this gas sufficiently well to distinguish differences from the predominately green spatial regions.

4. The Outflow in Henize 2-10

Regardless of whether an outflow occurring in Henize 2-10 escapes from the dark matter halo, it is instructive to consider whether the supernovae in the current burst can drive it. The $H\alpha$ luminosity of Henize 2-10, measured by Méndez et al. (1999) is 2.1×10^{41} erg s $^{-1}$ (uncorrected for extinction), leading to an implied current star formation rate of at least 1.8 M_\odot yr $^{-1}$ (Kennicutt 1989). For a Salpeter (1955) initial mass function with slope $\alpha = -2.35$ between 0.1 M_\odot and 100 M_\odot , the number of potential supernovae generated from an instantaneous burst producing 2.8×10^6 M_\odot of stars is about 15000 if all stars over 8 M_\odot end as supernovae. This is consistent with the 3750 SNRs already present, estimated independently from the nonthermal radio continuum by Méndez et al. (1999) or

the 5000 SNRs estimated by Allen et al. (1976). The implied current SN rate is one every 250 yrs. The supernova rate is equivalent to a mechanical energy injection rate varying from $\text{few} \times 10^{39}$ to 10^{41} erg s^{-1} over the first 10^7 yr, using the online instantaneous burst models of Leitherer et al. (1999). The total mechanical energy produced over this period would be 10^{55} erg. For continuous star formation models at a rate of $2 M_{\odot} \text{ yr}^{-1}$, the steady state mechanical energy injection rate is $\sim 3 \times 10^{41}$ erg s^{-1} or about 5×10^{55} erg over the last 10 Myr. These should be regarded as a lower limits, as the mid-IR measurement of the SF rate is nearly $7 M_{\odot} \text{ yr}^{-1}$. However, this rate is unsustainable for any extended duration in such a small galaxy. At this rate all molecular gas in the galaxy would be consumed in 40 Myr.

We have estimated the mechanical energy contained in the three H α shells observed to the NE and SW of the nucleus, adopting the Méndez et al. (1999) (projected) expansion speeds of 60 to ~ 300 km s^{-1} . These shells have a combined H α luminosity of $\sim 1 \times 10^{40}$ erg s^{-1} based on the fluxes measured on the H α images of Méndez et al. (1999), scaled to 9.8 Mpc. For an assumed density of $n_e = n_H = 100 \text{ cm}^{-3}$ and temperature of 10^4 K, the case B H α recombination coefficients and emissivities power of Hummer & Storey (1987) lead to a shell mass of $3.5 \times 10^5 M_{\odot}$, given a correction factor of 1.4 for helium. This implies a shell kinetic energy of $E_{kin} = 1.26 \times 10^{52} [v_{60}]^2$ erg, where v_{60} is the expansion speed in units of 60 km s^{-1} . For a bubble expansion speed of 300 km s^{-1} , this implies a maximum kinetic energy of 3.1×10^{53} erg. Such kinetic energies would be easily achieved given the magnitude of the star formation burst estimated above. Additional thermal energy, E_{th} , contained in the plasma can be estimated by adopting a volume for the hot gas (29 kpc 3), a mean density (0.01 cm^{-3} derived via the X-ray model normalization), and a mean energy per particle (0.7 keV). In this manner we find $E_{th} = 4 \times 10^{54}$ erg, i.e., a large fraction (up to 50%) of the total energy estimated to have been generated in the recent burst of star formation, if the lower limit of $2 M_{\odot} \text{ yr}^{-1}$ is adopted as an average SF rate. Adopting the larger IR-based SFR leads to a thermal energy reservoir that is $\sim 15\%$ of the total energy generated by recent star formation.

The poorly resolved rotation curve, ambiguous morphology, and unconstrained inclination of the H I in Henize 2-10 preclude a precise estimate of the escape velocity. Using the 21-cm L-V diagram from Kobulnicky et al. (1995), we estimate a dynamical mass of $2.94 \times 10^9 / \sin^2 i M_{\odot}$ within a radius of 2100 pc, or a halo mass of $11.8 \times 10^9 M_{\odot}$ for intermediate inclination, $i \approx 30$ degrees. Following Ferrara & Tolstoy (2000), we approximate the dark matter halo with a modified isothermal sphere. The halo scale radius is ~ 4.8 kpc. In this model, the escape velocity at 1.2 kpc is ~ 150 km s^{-1} . Only the highest-velocity component of the interstellar absorption trough (Schwartz 2005; Schwartz et al. 2006) reveals low-ionization gas exceeding this escape velocity. The location of this material along the line-of-sight is unconstrained, but even if it resides at 2.1 kpc or more, this component

represents a small fraction of the interstellar gas mass. The $H\alpha$ velocities Méndez et al. (1999) also reveal low-ionization gas at speeds exceeding the escape velocity, but these high speeds are measured about 0.6 kpc east of knot A. While some loss of low-ionization material appears likely, we find no direct evidence that the bulk of the interstellar gas will escape from Henize 2-10. This is consistent with the conclusions of Strickland et al. (2000) who found that starbursts were efficient at expelling metals but not the cool ISM. If the hotter plasma component, 0.6–0.8 keV in Table 4, represents the post-shock emission from an even hotter wind, then that wind has a velocity in the 790 to 900 km s⁻¹ range. Since we detect the shock emission out to 2.1 kpc, then this wind material appears likely to escape the dark halo. This finding suggests a high fraction of the metal yield from the starburst is ejected. That Henize 2-10 harbors a galactic wind is not surprising considering the very high intensity of star formation; the areal star formation rate exceeds 2 M_⊙ yr⁻¹ kpc⁻², which is well above the threshold suggested for winds (Heckman 2002), and may be as much as a factor of three higher, allowing for extinction.

5. Conclusions

X-ray imaging of Henize 2-10 has revealed a nuclear X-ray source with a probable luminosity exceeding 10⁴⁰ erg s⁻¹, suggesting the presence of an accreting black hole within the central 1'' (50 pc) with a mass of > 50 M_⊙. This source is coincident with a compact non-thermal radio source that, based on its non-detection in milliarcsec VLBA data, may be extended over scales of a few tens of pc. The angular size, luminosity, and ratio of radio to X-ray fluxes are consistent with properties of ULX sources and low-luminosity AGN in other galaxies.

We identify 33 compact X-ray sources in the *Chandra* field. Seven of these appear to be associated with He2-10 and may be luminous X-ray binaries (2–3) or peaks in the diffuse emission (4). Seven additional sources are likely to be foreground Galactic stars while eighteen sources are probable background AGN. These latter objects may constitute good probes of the ISM in and around He 2-10 if their UV fluxes are sufficiently large for studies with the *Hubble Space Telescope Cosmic Origins Spectrograph*.

Diffuse X-ray emission from Henize 2-10 accounts for 84% of the X-ray photons in the 0.3–6.0 keV bandpass, and 98% of the photons at intermediate energies (0.7–1.1 keV). The unabsorbed 0.3–6.0 keV X-ray luminosity of the diffuse ISM component is 1.0 × 10⁴⁰ erg s⁻¹ for the adopted distance of 9.8 Mpc. Although the data are insufficient to place strong constraints on the chemical properties, the X-ray spectrum is well fit by either a solar-composition two-temperature plasma with kT₁=0.69 keV and kT₂=0.19 keV or a sin-

gle temperature plasma with α/Fe ratios enhanced to ~ 2.7 times the solar value. Both interpretations have precedents in studies of other starburst galaxies.

We compare, for the first time, the distributions of the cold molecular, warm atomic, warm ionized, and hot coronal medium in He 2-10. The X-ray and $\text{H}\alpha$ emission follow a very similar radial surface brightness profile out to $30''$ (1.5 kpc). While both components extend far above and below the nuclear molecular “disk”, neither is detected at radii beyond the $8 \times 10^{20} \text{ cm}^{-2}$ H I contour. Unlike larger starburst spiral galaxies, no prominent outflow cones or extra-planar bubbles are observed beyond the neutral gas layer. To the surface brightness levels currently probed by X-ray and $\text{H}\alpha$ observations, the warm ionized and hot components lie well within the projected H I envelope. The absence of any systematic compilation of X-ray and H I distributions in dwarf galaxies makes it unclear whether He 2-10 is anomalous in this regard. Evidence for high-velocity outflows in low-ionization tracers is tenuous, suggesting that it is unlikely that large fraction of the neutral gas is presently being removed from the galaxy. However, the energy of the hot X-ray medium is $E_{th} = 4 \times 10^{54}$ erg. This constitutes a significant fraction of the energy estimated to have been generated in the recent starburst and a reservoir for the continuing development of a global wind. The high areal density of star formation can be reconciled with the lack of prominent outflow signatures if Henize 2-10 is in the very early stages of developing a galactic wind.

We thank Cesar Esteban for providing the $\text{H}\alpha$ image of Henize 2-10. We thank Karl Gebhardt for a timely communication about black holes in low-mass galaxies. Insightful remarks from an anonymous referee improved this manuscript. H. A. K acknowledges support from NASA through grant NRA-00-01-LTSA-052. C. L. M. acknowledges support from NASA through grant G01-2097X, the David and Lucile Packard Foundation, and from the National Science Foundation under contract 0808161.

Facilities: Chandra (), WIYN (), Keck(HIRES)

REFERENCES

- Allen, D. A., Wright, A. E., & Goss, W. M. 1976, MNRAS, 177, 91
- Baas, F., Israel, F. P., & Koornneef, J. 1994, A&A, 284, 403
- Beck, S. C., Kelly, D. M., & Lacy, J. H. 1997, AJ, 114, 585
- Berghea, C. T., Weaver, K. A., Colbert, E. J. M., & Roberts, T. P. 2008, ApJ, 687, 471
- Bohlin, R. C., Savage, B. D., & Drake, J. F. 1978, ApJ, 224, 132

- Cabanac, R. A., Vanzi, L., & Sauvage, M. 2005, *ApJ*, 631, 252
- Cagnoni, I., Turolla, R., Treves, A., Huang, J.-S., Kim, D. W., Elvis, M., Celotti, A. 2003, *ApJ*, 582, 654
- Calzetti, D., et al. 2007, *ApJ*, 666, 870
- Chandar, R., Leitherer, C., Tremonti, C., & Calzetti, D. 2003, *ApJ*, 586, 939
- Colbert, E. J. M. & Mushotzky, R. F. 1999, *ApJ*, 519, 89
- Colbert, E. J. M. & Ptak, A. F. 2002, *ApJS*, 143, 25
- Conti, P. 1991, *ApJ*, 377, 115
- Conti, P. S., & Vacca, W. D. 1994, *ApJ*, 423, L97
- Darling, J., Brogan, C., & Johnson, K. 2008, *ApJ*, 685, L39
- de Vaucouleurs, G, de Vaucouleurs, A., & Corwin, H. G., Buta, R., Paturel, G., & Fouqué, P. 1991, *Third Reference Catalog of Bright Galaxies*, Springer, New York (RC3)
- Engelbracht, C. W., Gordon, K. D., Rieke, G. H., Werner, M. W., Dale, D. A., & Latter, W. B. 2005, *ApJ*, 628, L29
- Ferrara, A., & Tolstoy, E. 2000, *MNRAS*, 313, 291
- Hartmann, D., & Burton, W. B. 1996, *Atlas of Galactic Neutral Hydrogen*, Cambridge University Press,
- Gebhardt, K. et al. 2000, *ApJ*, 539, L13
- Grimes, J. P., Heckman, T., Strickland, D., & Ptak, A. 2005, *ApJ*, 628, 187
- Guzman, R., Jangren, A., Koo, D. C., Bershady, M. A. & Simard, L. 1998, *ApJ*, 495, L13
- Guzman, R., Koo, D. C., Faber, S. M., Illingworth, G. D., Takamiya, M., Kron, R. G., & Bershady, M. A. 1996, *ApJ*, 460, L5
- Heckman, T. M. 2002, *Extragalactic Gas at Low Redshift*, 254, 292
- Hummer, D. G., & Storey, P. J. 1987, *MNRAS*, 224, 801
- Irwin, J. A., Bregman, J. N., & Athey, A. E. 2004, *ApJ*, 601, L143
- Johnson, K. E., Leitherer, C., Vacca, W. D., & Conti, P. S. 2000, *ApJ*, 120, 1273

- Johnson, K. E. & Kobulnicky, H. A. 2003, *ApJ*, 597, 923
- Johansson, I. 1987, *A&A*, 182, 179
- Kawara, K., Nishida, M., & Phillips, M. M. 1989, *ApJ*, 337, 230
- Kennicutt, R. C. 1989, *ApJ*, 344, 685
- Kim, M., Wilkes, B. J., Kim, D.-W., Green, P. J., Barkhouse, W. A., Lee, M. G., Silverman, J. D., & Tananbaum, H. D. 2007, *ApJ*, 659, 29
- King, A. R. 2009, *MNRAS*, 393, L41
- King, A. R., Davies, M. B., Ward, M. J., Fabbiano, G., Elvis, M. 2001, *ApJ*, 552, 109
- Körding, E., Falcke, H., Markoff, S. 2002, *A&A*, 382, 13
- Kobulnicky, H. A., & Johnson, K. 1999, *ApJ*, 527, 154
- Kobulnicky, H. A., Dickey, J. M., Sargent, A. I., Hogg, D. E., & Conti, P. S. 1995, *AJ*, 110, 116
- Kobulnicky, H. A., Kennicutt, R. C., & Pizagno, J. L. 1999, *ApJ*, 514, 544
- Koo, D. C., Guzman, R., Faber, S. M., Illingworth, G. D. Bershadsky, M. A., Kron, R. G., Krautter, J., et al. 1999, *A&A*, 350, 743
- Lang, C. C., Kaaret, P., Corbel, S., & Mercer, A. 2007, *ApJ*, 666, 79
- Leitherer, C. et al. 1999, *ApJS*, 123, 3
- Marlowe, A. T., Heckman, T. M., Wyse, R. F. G., & Schommer, R. 1995, *ApJ*, 438, 563
- Martin, C. L. 1998, *ApJ*, 506, 222
- Martin, C. L., & Bouché, N. 2009, *ApJ*, 703, 1394
- Martin, C. L., Kobulnicky, H. A., & Heckman, T. M. 2002, *ApJ*, 574, 663
- Marzke, R. O., da Costa, L. N., Pellegrini, P. S., Willmer, C. N. A., Geller, M. J. 1998, *ApJ*, 503, 617
- Meier, D. S. Turner, J. L., Crosthwaite, L. P. Beck, S. C. 2001, *AJ*, 121, 740

- Méndez, D. I., Esteban, C., Filipović, M. D., Ehle, M., Haberl, F., Pietsch, W., & Haynes, R. F. 1999, *A&A*, 349, 801
- Merloni, A., Heinz, S., & Di Matteo, T. 2002, *MNRAS*, 345, 1057
- Miller, M. M., & Colbert, E. J. M. 2004, *IJMPD*, 13, 1
- Miller, N. A., Mushotzky, R. F., & Neff, S. G. 2005, *ApJ*, 623, L109
- Moretti, A., Campana, S., Lazzati, D., & Tagliaferri, G. 2003, *ApJ*, 588, 696
- Mushotzky, R. F., Cowie, L. L., Barger, A. J., & Arnaud, K. A. 2000, *Nature*, 404, 459
- Neff, S. G., Ulvestad, J. S., & Campion, S. D. 2003, *ApJ*, 599, 1043
- Ott, J., Walter, F., & Brinks, E. 2005, *MNRAS*, 358, 1453
- Phillips, M. M., Aitken, D. K., & Roche, P. F. 1984, *MNRAS*, 207, 25
- Phillips, A. C., Guzman, R., Gallego, J., Koo, D. C., Lowenthal, J. D., Vogt, N. P., Faber, S. M., & Illingworth, G. D. 1997, *ApJ*, 489, 543
- Ptak, A., Colbert, E., van der Marel, R. P., Roye, E., Heckman, T., & Towne, B. 2006, *ApJS*, 166, 154
- Ramsey, C. J., Williams, R. M., Gruendl, R. A., Chen, C.-H. R., Chu, Y.-H., & Wang, Q. D. 2006, *ApJ*, 641, 241
- Rappaport, S. A., Podsiadlowski, P., & Pfahl, E. 2005, *MNRAS*, 356, 401
- Remillard, R. A., & McClintock, J. E. 2006, *ARA&A*, 44, 49
- Roberts, T. P., Warwick, R. S., Ward, M. J., & Goad, M. R. 2004, *MNRAS*, 349, 1193
- Salpeter, E. E. 1955, *ApJ*, 121, 161
- Santangelo, G., Testi, L., Gregorini, L., Leurini, S., Vanzi, L., Walmsley, C. M., & Wilner, D. J. 2009, *A&A*, 501, 495
- Schwartz, C. 2005, PhD Dissertation, University of California, Santa Barbara
- Schwartz, C. M., Martin, C. L., Chandar, R., Leitherer, C., Heckman, T. M., & Oey, M. S. 2006, *ApJ*, 646, 858
- Strickland, D. K., Heckman, T. M., Weaver, K. A. & Dahlem, M. 2000, *AJ*, 120, 2965

- Strickland, D. K., Heckman, T. M., Colbert, E. J. M., Hoopes, C. G., & Weaver, K. A. 2004, *ApJS*, 151, 193
- Summers, L. K., Stevens, I. R., Strickland, D. K., & Heckman, T. M. 2004, *MNRAS*, 351, 1
- Swartz, D. A., Ghosh, K. K., Tennant, A. F., Wu, K. 2004, *ApJS*, 154, 519
- Terashima, Y., & Wilson, A. S. 2003, *ApJ*, 583, 145
- Tremaine, S., et al. 2002, *ApJ*, 574, 740
- Ulvestad, J. S., Greene, J. E., & Ho, L. C. 2007, *ApJ*, 661, L151
- Ulvestad, J. S., Johnson, K. E., & Neff, S. G. 2007, *AJ*, 133, 1868
- Vacca, W. D., & Conti, P. S. 1992, *ApJ*, 401, 543
- Vacca, W. D., Johnson, K. E., & Conti, P. S. 2002, *AJ*, 123, 772
- Wilms, J., Allen, A., & McCray, R. 2000, *ApJ*, 542, 914
- Winter, L. M., Mushotzky, R. F., & Reynolds, C. S. 2006, *ApJ*, 649, 730
- Zezas, A. & Fabbiano, G. 2002, *ApJ*, 577, 726

Table 1. Henize 2-10 X-ray Point Sources

ID (1)	CXO Designation (2)	R.A. (2000) (3)	Decl. (2000) (4)	C_{tot} (5)	C_S (6)	C_M (7)	C_H (8)	$Rat.PSF$ (9)	R (mag) (10)	$\log(f_X/f_V)$ (11)	Type (12)	
1	CXOU083615.1-262433	8 36 15.12	-26 24 33.7	210.0±15.7	13.1± 4.2	30.5± 7.1	159.4± 13.1	4.4	>19	...	>0.2 XRB/AGN?	
2	CXOU083616.0-262430	8 36 16.02	-26 24 30.6	23.6± 5.9	3.6± 2.3	4.4± 3.1	13.7± 4.3	2.6	>21.5	...	>0.3 XRB	
3	CXOU083615.8-262434	8 36 15.82	-26 24 34.1	45.1± 7.4	1.7± 1.7	7.6± 3.5	36.0± 6.3	3.0	>21.5	...	>0.5 XRB	
4	CXOU083616.5-262137	8 36 16.51	-26 25 37.6	4.9± 2.2	-0.0± 0.0	2.0± 1.4	3.0± 1.7	1.0	>21.5	...	> -0.4 AGN	
5	CXOU083612.3-262405	8 36 12.27	-26 24 05.5	52.8± 7.3	2.0± 1.4	16.0± 4.0	34.9± 5.9	1.9	19.5	0.4	-0.2 AGN	
6	CXOU083612.2-262322	8 36 12.17	-26 23 22.2	32.2± 5.7	3.8± 2.0	7.0± 2.6	21.8± 4.7	1.8	19.6	0.4	-0.4 AGN	
7	CXOU083600.3-262138	8 36 00.34	-26 21 37.6	446.8±21.3	106.8±10.4	203.5± 14.3	138.1± 11.8	1.2	10.5	0.4	-2.8 Star	
8	CXOU083625.0-262302	8 36 25.04	-26 23 02.1	23.5± 4.9	8.8± 3.0	13.0± 3.6	1.9± 1.4	1.3	16.4	0.4	-1.7 Star	
9	CXOU083616.9-261840	8 36 16.87	-26 18 40.3	94.9±10.0	29.7± 5.5	34.7± 5.9	29.5± 5.6	1.3	14.9	0.4	-1.7 Star	
10	CXOU083613.5-262543	8 36 13.47	-26 25 43.8	9.4± 3.2	-0.0± 0.0	-0.0± 0.0	9.8± 3.2	2.2	>21.5	...	> -0.2 AGN	
11	CXOU083612.2-262018	8 36 12.28	-26 20 18.0	17.7± 4.4	6.9± 2.6	7.0± 2.6	4.7± 2.2	0.9	>21.5	...	> 0.1 AGN	
12	CXOU083610.1-262355	8 36 10.12	-26 23 55.3	6.7± 2.6	2.0± 1.4	3.0± 1.7	1.9± 1.4	1.6	>21.5	...	> -0.3 AGN	
13	CXOU083609.6-262630	8 36 09.66	-26 26 30.4	11.7± 3.5	2.0± 1.4	6.0± 2.4	2.9± 1.7	1.5	14.3	0.4	-2.9 Star	
14	CXOU083603.0-262715	8 36 03.05	-26 27 15.6	25.3± 5.1	6.6± 2.7	13.0± 3.6	5.9± 2.5	1.1	16.2	0.4	-1.8 Star	
15	CXOU083630.2-262252	8 36 30.29	-26 22 52.7	5.4± 2.5	0.8± 1.0	1.9± 1.4	2.8± 1.7	1.1	12.9	0.4	-3.8 Star	
16	CXOU083630.0-262533	8 36 30.13	-26 25 33.9	3.9± 2.0	-0.0± 0.0	1.0± 1.0	2.9± 1.7	0.4	18.1	0.4	-1.8 Star	
17	CXOU083625.4-262103	8 36 25.57	-26 21 04.6	9.0± 3.2	-0.3± 0.2	2.8± 1.7	5.7± 2.5	0.9	>21.5	...	> -0.2 AGN	
18	CXOU083614.3-261833	8 36 14.40	-26 18 33.7	36.1± 6.7	4.8± 2.5	11.6± 3.5	16.8± 4.3	1.2	>21.5	...	>0.4 AGN	
19	CXOU083613.0-261904	8 36 13.11	-26 19 04.4	91.6± 9.9	19.5± 4.5	20.3± 4.6	47.3± 6.9	1.2	>21.5	...	>0.8 AGN	
20	CXOU083611.7-262133	8 36 11.75	-26 21 33.2	3.7± 2.0	1.0± 1.0	1.0± 1.0	1.8± 1.4	0.6	>21.5	...	> -0.5 AGN	
21	CXOU083608.2-262035	8 36 08.18	-26 20 35.1	6.7± 2.6	-0.1± 0.1	3.9± 2.0	2.9± 1.7	0.4	>21.5	...	> -0.3 AGN	
22	CXOU083604.0-261953	8 36 03.91	-26 19 54.6	5.6± 2.7	1.8± 1.4	2.7± 1.7	1.3± 1.4	0.5	>21.5	...	> -0.4 AGN	
23	CXOU083559.2-262711	8 35 59.18	-26 27 10.8	8.6± 3.0	-0.1± 0.1	2.9± 1.7	5.9± 2.5	1.0	>21.5	...	> -0.2 AGN	
24	CXOU083552.2-262154	8 35 52.17	-26 21 54.6	8.5± 3.2	0.8± 1.0	1.9± 1.4	5.0± 2.5	0.4	>21.5	...	> -0.2 AGN	
25	CXOU083626.6-262157	8 36 26.59	-26 21 56.6	8.0± 3.0	-0.3± 0.2	0.0± 0.0	6.7± 2.7	1.0	>21.5	...	> -0.2 AGN	
26	CXOU083602.8-261912	8 36 03.10	-26 19 13.4	19.5± 4.9	2.7± 1.8	3.7± 2.0	13.1± 3.8	1.0	>21.5	...	>0.2 AGN	
27	CXOU083602.1-261850	8 36 02.03	-26 18 50.4	14.4± 4.4	5.4± 2.5	2.4± 1.8	5.6± 2.7	0.9	>21.5	...	>0.0 AGN	
28	CXOU083559.3-261853	8 35 59.29	-26 18 52.6	4.4± 2.3	2.8± 1.7	-0.2± 0.2	1.0± 1.0	0.6	>21.5	...	> -0.5 AGN	
29	CXOU083559.1-262656	8 35 59.11	-26 26 56.2	4.3± 2.2	0.8± 1.0	0.9± 1.0	2.8± 1.7	0.6	>21.5	...	> -0.5 AGN	
30	CXOU083615.1-262437	8 36 15.12	-26 24 37.8	23.1±8.5	0.5±3.2	17.4±6.8	5.9±4.5	1.74	>19	Diffuse
31	CXOU083615.2-262434	8 36 15.22	-26 24 34.6	64.3±16.9	17.8±6.1	56.8±11.1	0.5±10.5	1.94	>19	Diffuse
32	CXOU083615.3-262433	8 36 15.33	-26 24 33.2	22.1±11.7	4±4.6	9.4±8.1	9.6±7.5	1.94	>19	Diffuse
33	CXOU083615.4-262435	8 36 15.40	-26 24 35.2	12.6±7.7	0.5±3	7.9±6.1	0.5±4.6	1.99	>19	Diffuse

References. — (1) Reference ID # for this paper; (2) *Chandra* X-Ray Observatory identifier; (3) J2000 Right Ascension from ACIS total band image; (4) J2000 Declination; (5) Background-subtracted X-ray counts for each source in the 20 ksec observation detected in the 0.3–6.0 keV band and 1σ uncertainty from photon statistics. The nominal count rate to energy flux conversion is $1 \text{ count s}^{-1} = 7.3 \times 10^{-12} \text{ erg s}^{-1} \text{ cm}^{-2}$ for a Galactic foreground of $1.0 \times 10^{20} \text{ cm}^{-2}$. (6) Counts in the 0.3–0.7 keV soft X-ray band. $1 \text{ count s}^{-1} = 6.6 \times 10^{-12} \text{ erg s}^{-1} \text{ cm}^{-2}$. (7) Counts in the 0.7–1.1 keV medium X-ray band. $1 \text{ count s}^{-1} = 3.3 \times 10^{-12} \text{ erg s}^{-1} \text{ cm}^{-2}$. (8) Counts in the 1.1–6 keV hard X-ray band. $1 \text{ count s}^{-1} = 8.8 \times 10^{-12} \text{ erg s}^{-1} \text{ cm}^{-2}$. (9) Ratio of source size to PSF size; (10) R-band magnitude of optical counterpart, if any, from either our R-band imaging; the 1σ uncertainty is typically 0.4 mag. (11) Log of the ratio of X-ray to optical flux, f_X/f_V : for this purpose we use $f_X(\text{erg s}^{-1} \text{ cm}^{-2}) = 5.1 \times 10^{-18} \times C_{tot}$ where C_{tot} is the number of detected photons from column 5 and $f_V(\text{erg s}^{-1} \text{ cm}^{-2}) = 1.7 \times 10^{-9} \times 2.5^{-R}$ where R is the R magnitude from column 10. (13) Probable source type based on X-ray, radio, optical fluxes or IDs. Objects with $\log(f_X/f_V) < -0.5$ we tentatively identify as stars; Objects with $\log(f_X/f_V) > -0.5$ we tentatively identify as probable AGN. Objects in the disk He 2-10 without optical ID we identify as probable X-ray binaries.

Table 2. Henize 2-10 X-ray Fluxes and Fractions

Band (keV)	Gross Cts	Flux	Point Source Cts	Net Diffuse Cts	Diffuse Fraction
(1)	(2)	(3)	(4)	(5)	(6)
0.3–6.0	1296±41	1.6×10^{-13}	202±17	1094±44	84%± 4%
1.1–6.0	464±26	5.8×10^{-14}	141±15	323±30	69%± 9%
0.7–1.1	657±27	8.4×10^{-14}	11± 8	646±28	98%± 4%
0.3–0.7	174±18	2.0×10^{-14}	9± 5	165±19	95%±11%

References. — (1) Bandpass; (2) Background-subtracted counts within 80'' diameter aperture; (3) Observed flux corresponding to count rate in column 2 in $\text{erg s}^{-1} \text{cm}^{-2}$ for best fitting models discussed in Section 3.; (4) Total counts in point sources 1, 6, and 7 from Table 1; (5) Background-subtracted net counts from diffuse emission ; (6) Fraction of flux from diffuse component

Table 3. Nuclear Source Spectral Fitting

Name	Model	N_{H_1}	N_{H_2}	kT	Γ	Norm ₁	Norm ₂	red. χ^2	d.o.f.	L_X
(1)	(2)	(3)	(4)	(5)	(6)	(7)	(8)	(9)	(10)	(11)
A	wabs(mekal+wabs*pow)	1.2±0.2	9.7±1.2	0.4#	4#	$1.1 \pm 0.2 \times 10^{-4}$	$24.3 \pm 7.6 \times 10^{-4}$	0.89	9	1.8×10^{41}
B	wabs(mekal+wabs*pow)	1.0±0.2	4.5±0.9	0.4#	2#	$1.1 \pm 0.9 \times 10^{-4}$	$1.0 \pm 0.3 \times 10^{-4}$	1.10	9	1.1×10^{40}
C	wabs(mekal+wabs*pow)	0.8±0.2	1.9±0.6	0.4#	1#	$0.6 \pm 0.6 \times 10^{-4}$	$0.2 \pm 0.1 \times 10^{-4}$	1.33	9	5.7×10^{39}

References. — (1) Model designation; (2) Xspec Model formulae; (3) Foreground absorbing column density for MEKAL component (10^{22}cm^{-2}); (4) Foreground absorbing column density for power law component intrinsic to Henize 2-10 (10^{22}cm^{-2}); (5) Temperature of the MEKAL component (keV) ; (6) Photon index of the power law component ; (8) Normalization of the MEKAL model in units of $10^{-5} \int 10^{-14} n_e n_H dV / 4\pi D^2$, where D is the distance to the source; (8) Normalization of the power law model ; (9) Reduced χ^2 of fit ; (10) Degrees of freedom in fit ; (11) Unabsorbed 0.3–6.0 keV luminosity in erg s^{-1} at a distance of 12.2 Mpc for an observed flux of $1.12 \times 10^{-11} \text{erg cm}^{-2} \text{s}^{-1}$; (#) Denotes parameters held fixed

Table 4. Diffuse Emission Spectral Fitting

ID	Aperture	Model	N_{H_0}	N_{H_1}	kT_1	α/H	α/Fe	Norm ₁	N_{H_2}	kT_2	Norm ₂	red. χ^2	d.o.f.	L_X
(1)	(2)	(3)	(4)	(5)	(6)	(7)	(8)	(9)	(10)	(11)	(12)	(13)	(14)	(15)
1	2–40''	wabs(wabs(mekal+mekal))	0.05 [#]	0.50±0.03	0.069±0.07	1 [#]	1 [#]	15.9±6	0.50±0.02	0.19±0.02	8.0±13	0.97	38	2.2×10^{40}
2	2–40''	wabs(wabs*mekal)	0.05 [#]	0.23±0.04	0.63±0.04	1 [#]	1 [#]	12.7±0.2	2.25	40	3.8×10^{39}
3	2–40''	wabs(wabs*mekal)	0.05 [#]	0.18±0.03	0.65±0.04	0.14±0.03	1 [#]	45.4±0.2	1.15	39	3.5×10^{39}
4	2–40''	wabs(wabs*vmekal)	0.05 [#]	0.10±0.03	0.64±0.04	0.77±0.4	2.7±0.5	20.4±0.2	0.95	38	3.0×10^{39}

References. — (1) Model ID; (2) Aperture; (3) Xspec Model formula; (4) Galactic foreground absorbing column density (10^{22} cm^{-2}); (5) Foreground absorbing column density for component intrinsic to Henize 2-10 (10^{22} cm^{-2}); (6) Temperature of the first MEKAL component (keV) ; (7) α -element abundance relative to solar ; (8) α/Fe abundance ratio relative to solar ; (9) Normalization of the MEKAL model in units of $10^{-5} \int 10^{-14} n_e n_H dV / 4\pi D^2$ where D is the distance to the source ; (10) Foreground absorbing column density for second component (10^{22} cm^{-2}); (11) Temperature of the second MEKAL component (keV) ; (12) Normalization of the second MEKAL model in units of $10^{-5} \int 10^{-14} n_e n_H dV / 4\pi D^2$; (13) Reduced χ^2 of fit ; (14) Degrees of freedom in fit ; (15) Unabsorbed 0.3–6.0 keV Luminosity in erg s^{-1} for a distance of 12.2 Mpc ; (#) Denotes parameters held fixed

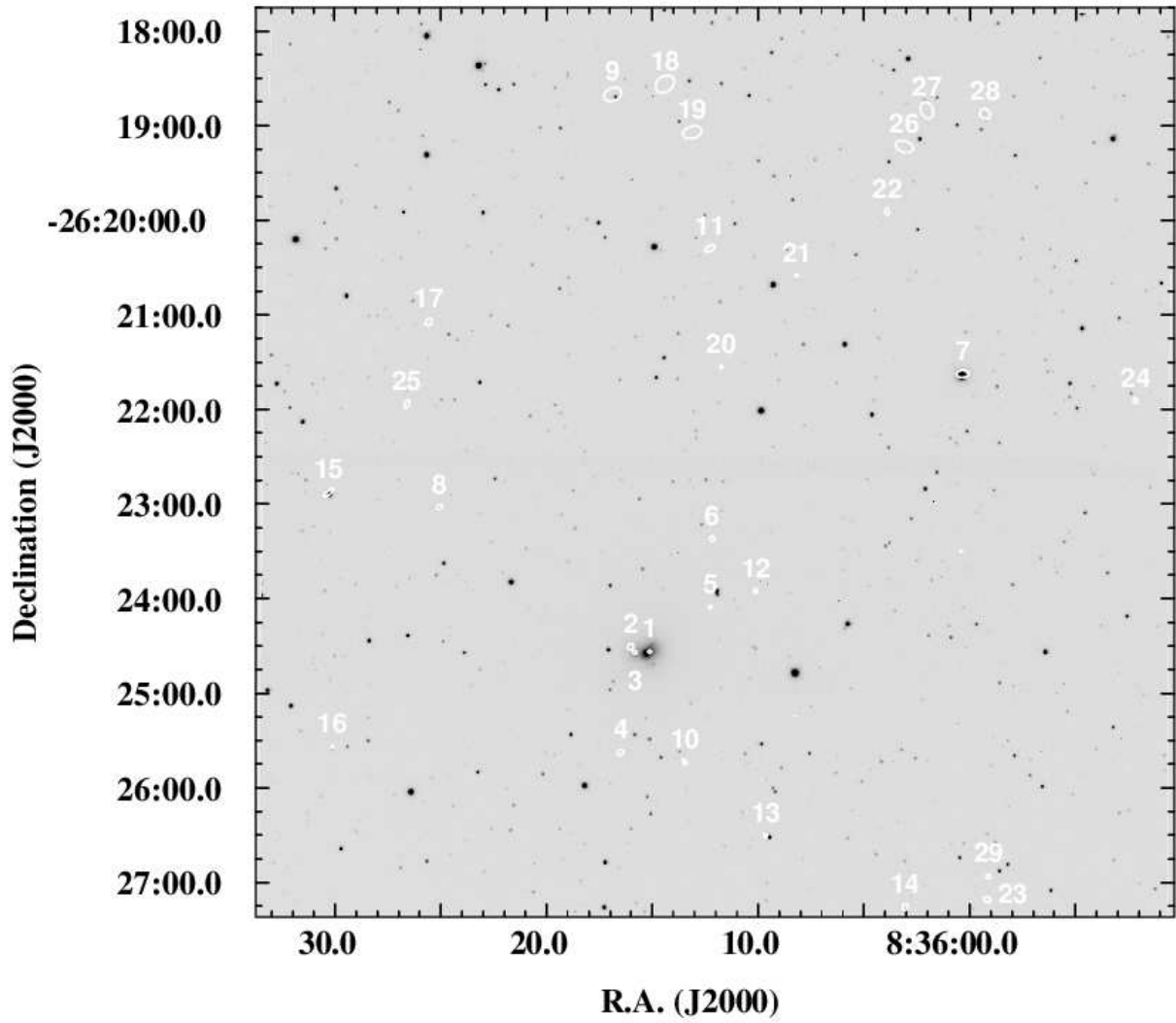


Fig. 1.— Grayscale optical 6550 Å image with compact X-ray sources (*numbered white ellipses*) detected in the 0.3 – 6 keV band near Henize 2-10. Object labels correspond to the X-ray sources listed in Table 1.

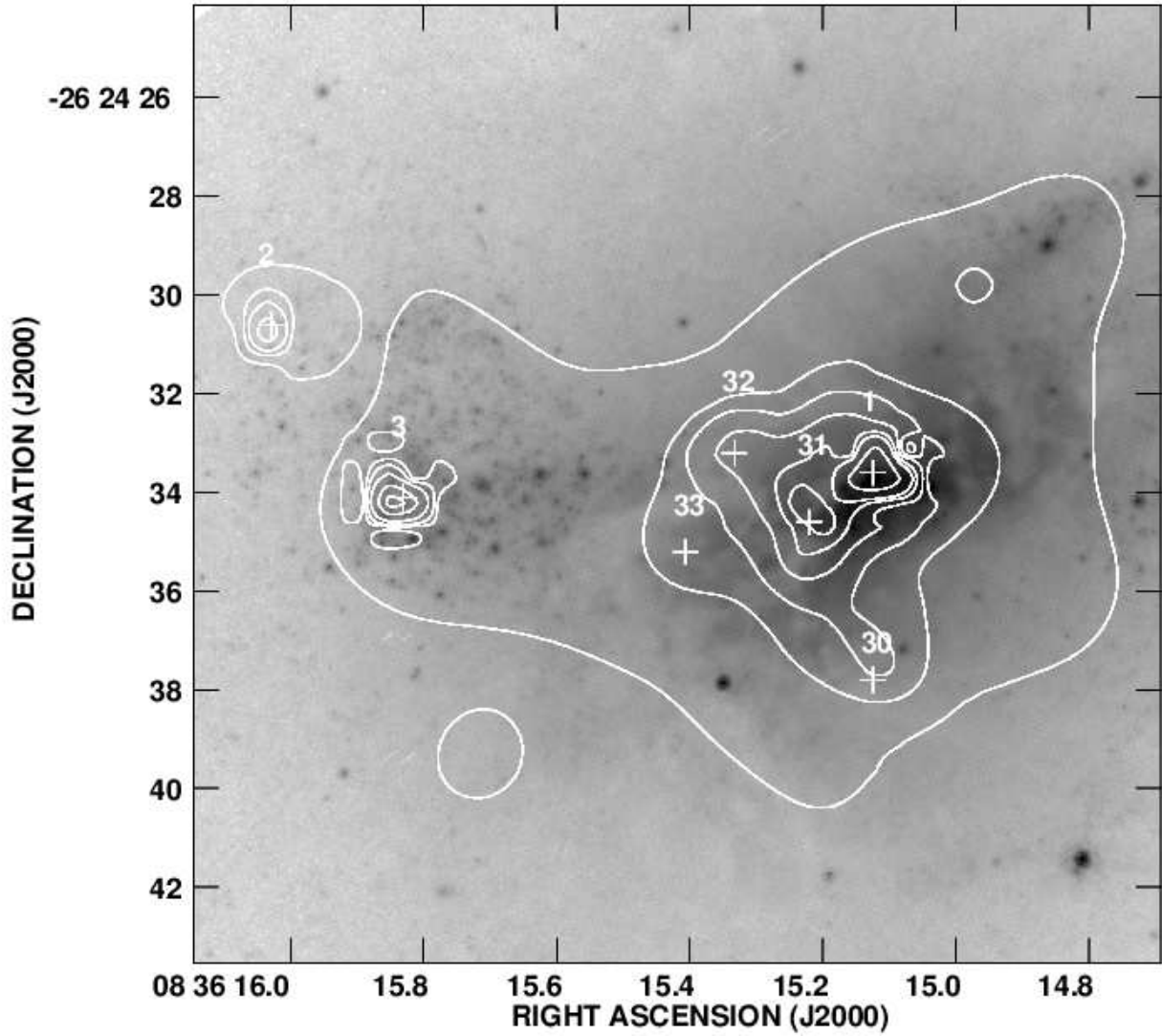


Fig. 2.— X-ray point sources (*white crosses*) near the nucleus of Henize 2-10. The grayscale shows a logarithmic representation of the Hubble Space Telescope F814W image from Johnson et al. (2000), and the contours show the adaptively-smoothed *Chandra* ACIS total band 0.3–6 keV image. Contours levels are drawn every factor of 2 at 0.42, 0.85, 1.7, 3.5, 7.0, 14.0, 28.0 photons $\text{s}^{-1} \text{arcmin}^{-2}$.

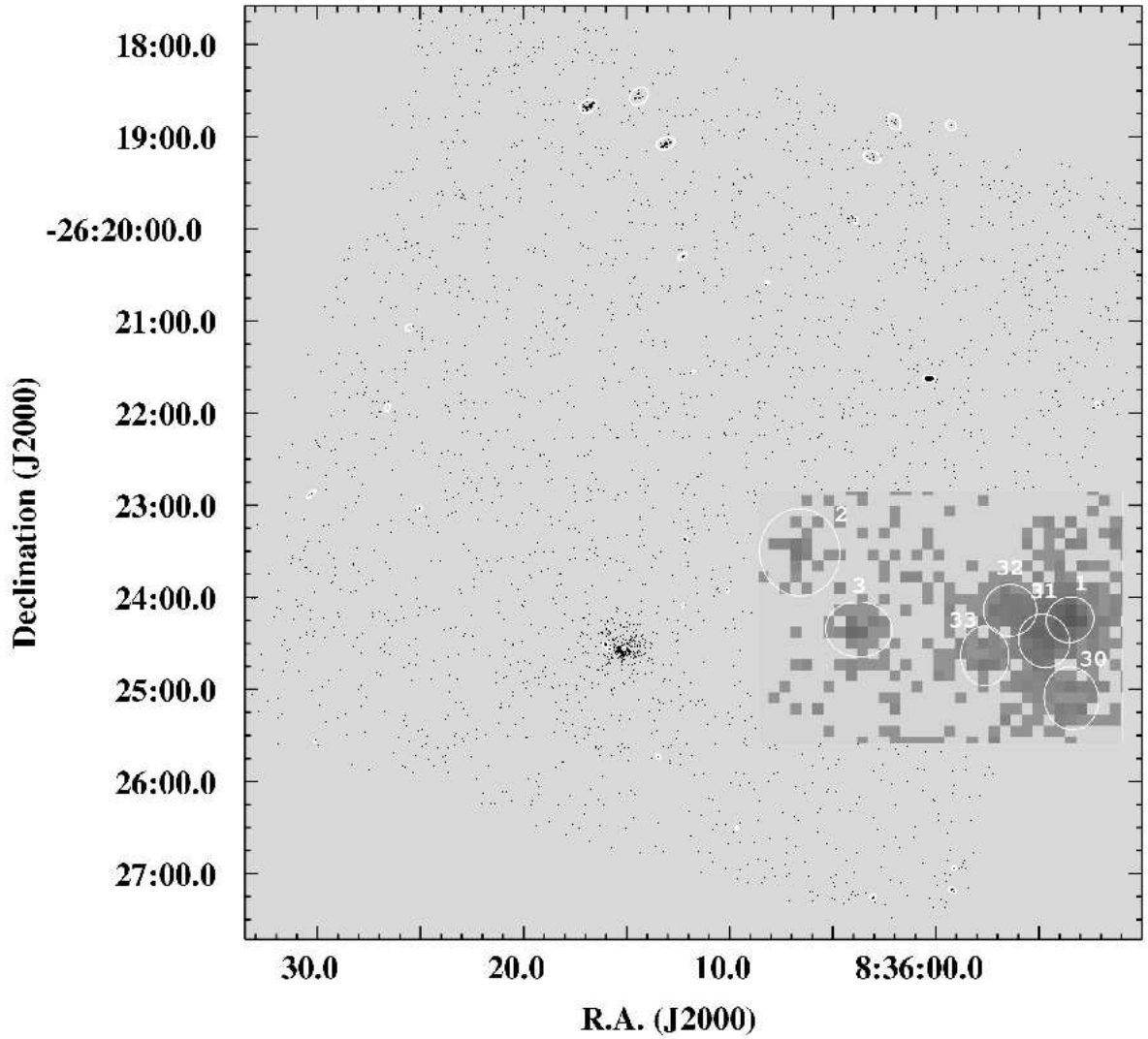


Fig. 3.— An unsmoothed total band 0.3 – 6 keV X-ray image the ACIS S-3 chip with He 2-10 near the center. White ellipses are the same as in Figure 1. The inset shows a magnified view near the nucleus of He 2-10 with objects 1,2,3 and 30–33 numbered.

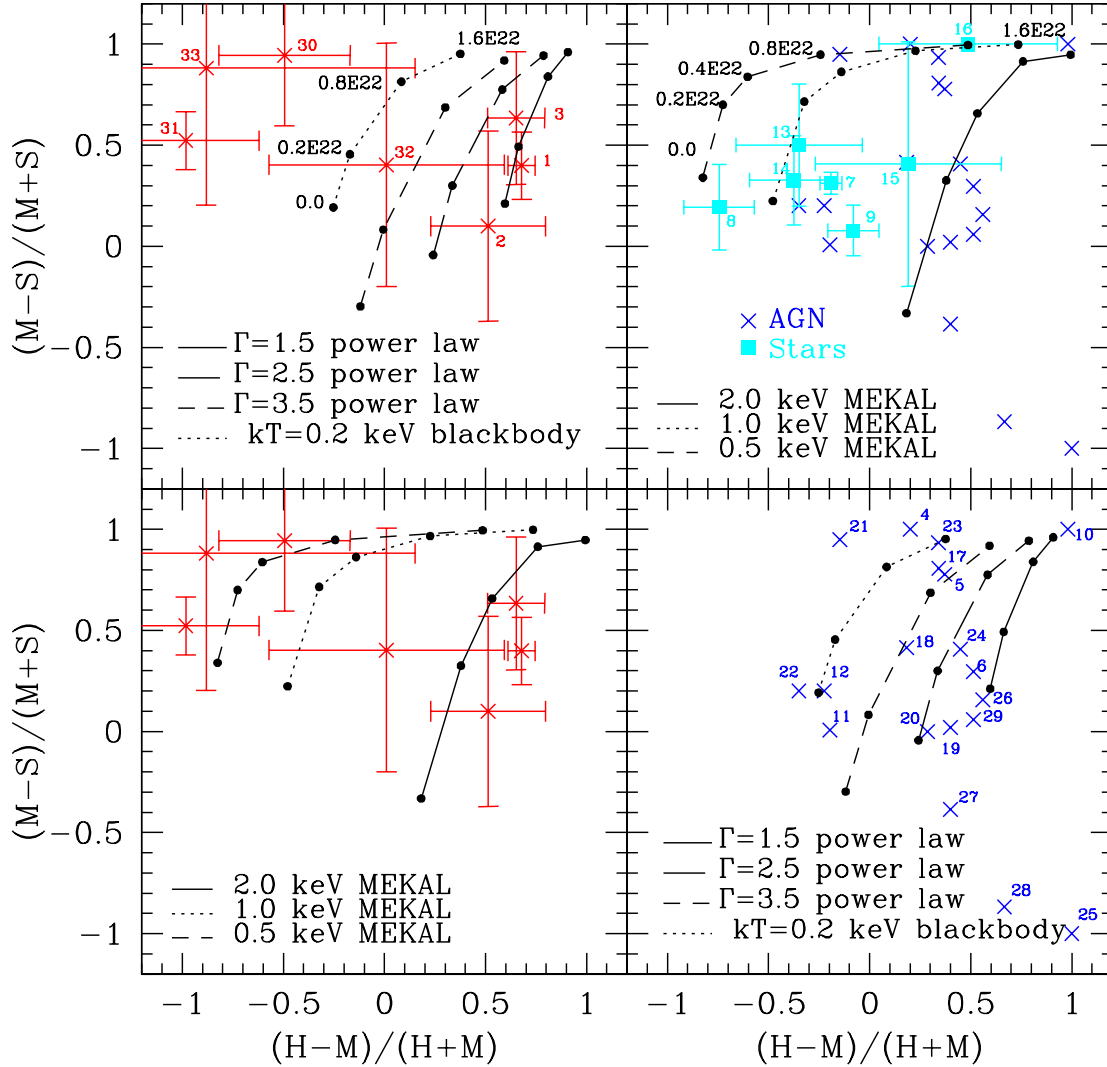


Fig. 4.— Two-color diagram for X-ray point sources. Lines represent the colors of model spectra. Upper left: The seven sources projected against the nucleus of Henize 2-10. Power laws with photon indices of $\Gamma=1.5$, $\Gamma=2.5$, $\Gamma=3.5$, and a blackbody spectrum with a temperature $kT=0.2$ keV are shown for several foreground H I column densities of 0.0, 0.2×10^{22} , 0.8×10^{22} , and 1.6×10^{22} cm^{-2} . Lower left: The seven compact sources. MEKAL thermal plasma models with temperatures $kT=0.5$, $kT=1.0$ and $kT=2.0$ keV for several foreground H I column densities are shown. Upper right and lower right: Other X-ray sources which lie outside the disk of He 2-10. Thermal plasma models and power law models for a range of column densities are shown. Filled squares denotes objects identified as probable stars in Table 1 on the basis of X-ray to optical fluxes, $\log(f_X/f_V) < -0.5$, while crosses denote probable AGN with $\log(f_X/f_V) > -0.5$. Error bars are omitted on AGN for clarity.

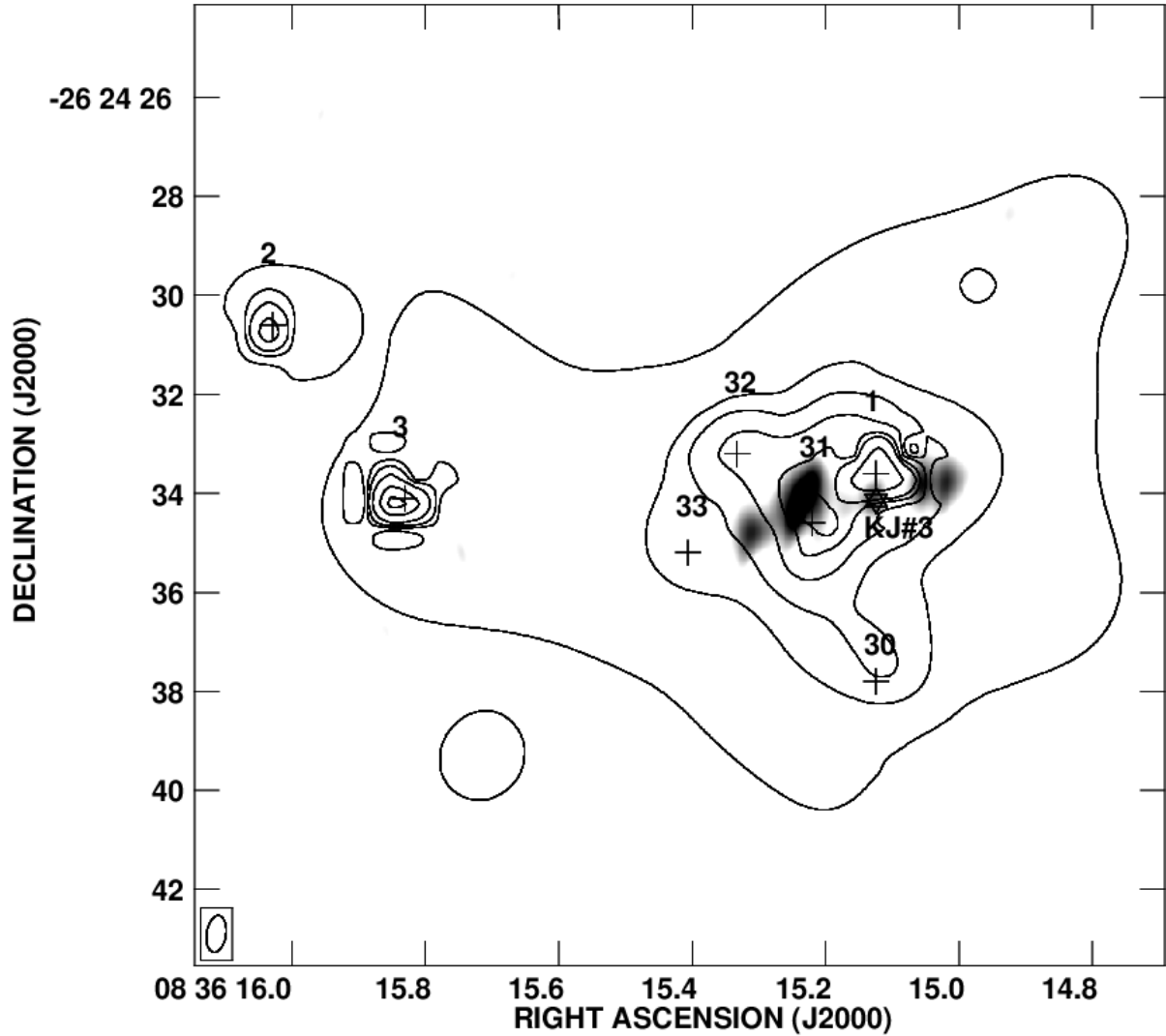


Fig. 5.— X-ray *Chandra* ACIS total band 0.3–6 keV image of the nucleus of Henize 2-10 with contours as in Figure 2. The grayscale shows a logarithmic representation of the 2 cm Very Large Array radio continuum maps from Kobulnicky & Johnson (1999). A star marks the position of radio source KJ3 from Kobulnicky & Johnson (1999) which lies 0.25" south, but within the positional uncertainties of the dominant X-ray point source #1.

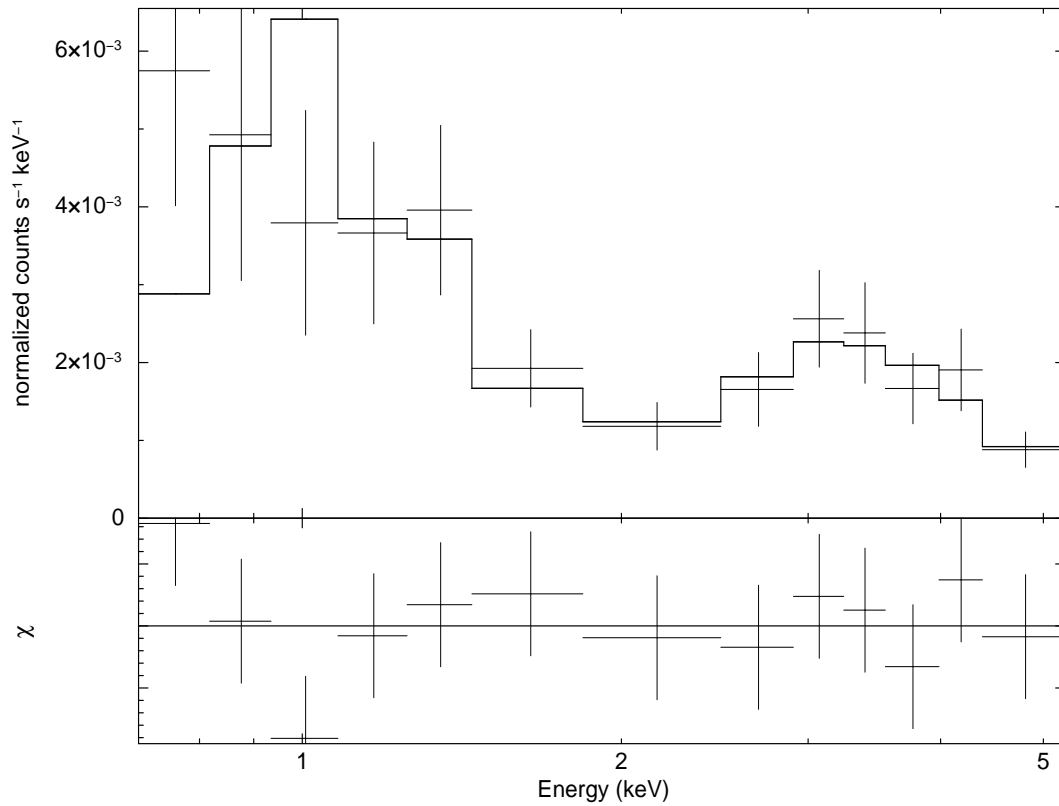


Fig. 6.— X-ray spectrum of the nuclear point source #1 and best-fit absorbed power law+MEKAL model and residuals (Model A in Table 3). Error bars represent 1-sigma uncertainties. The fit shown is for power law photon index $\Gamma = 4$, plasma temperature $kT = 0.4$ keV and foreground absorbing column density of 9.7×10^{22} cm⁻².

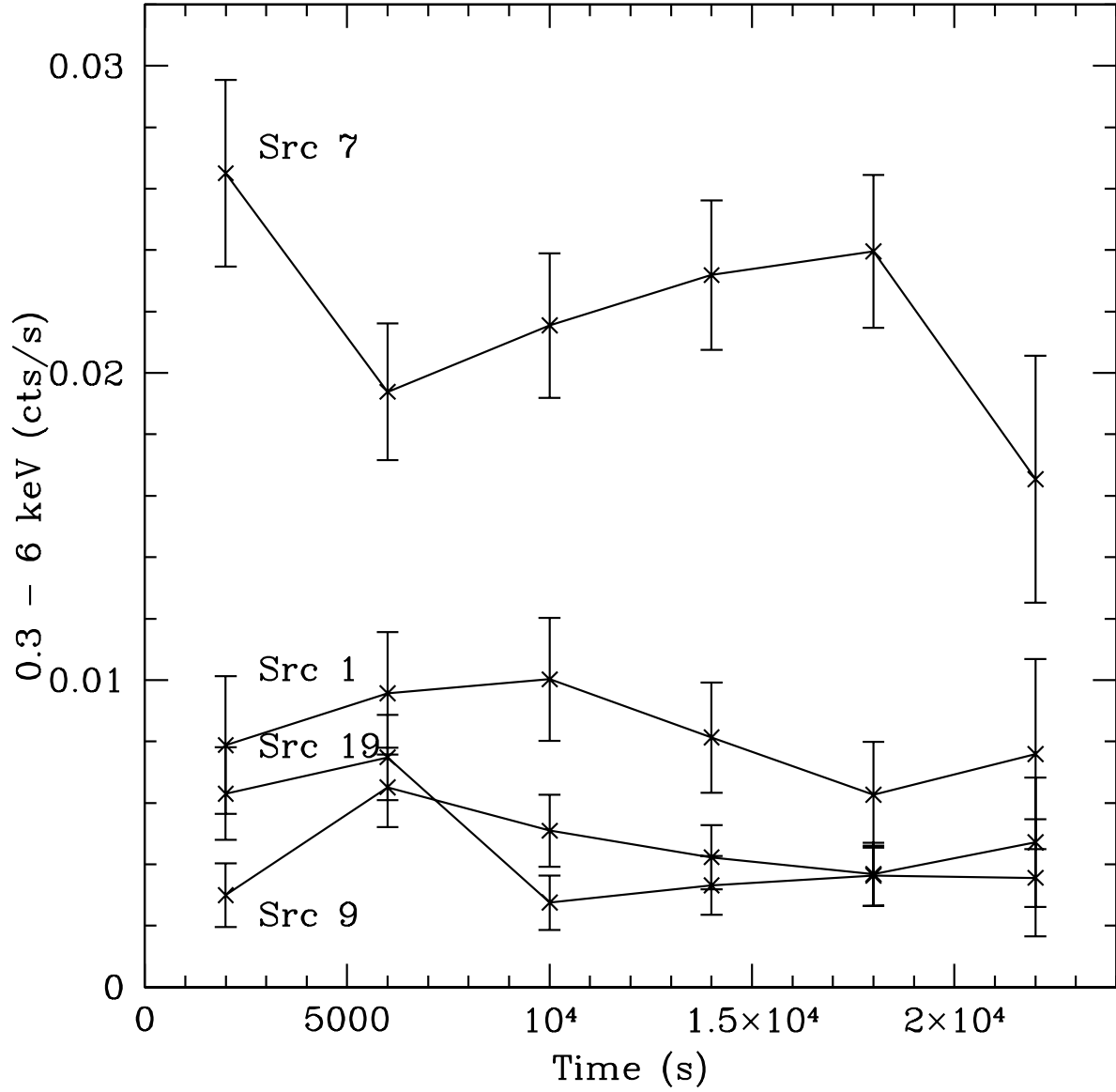


Fig. 7.— X-ray 0.3–6.0 keV light curve of the nuclear point source #1 and three other field X-ray sources from Table 1.

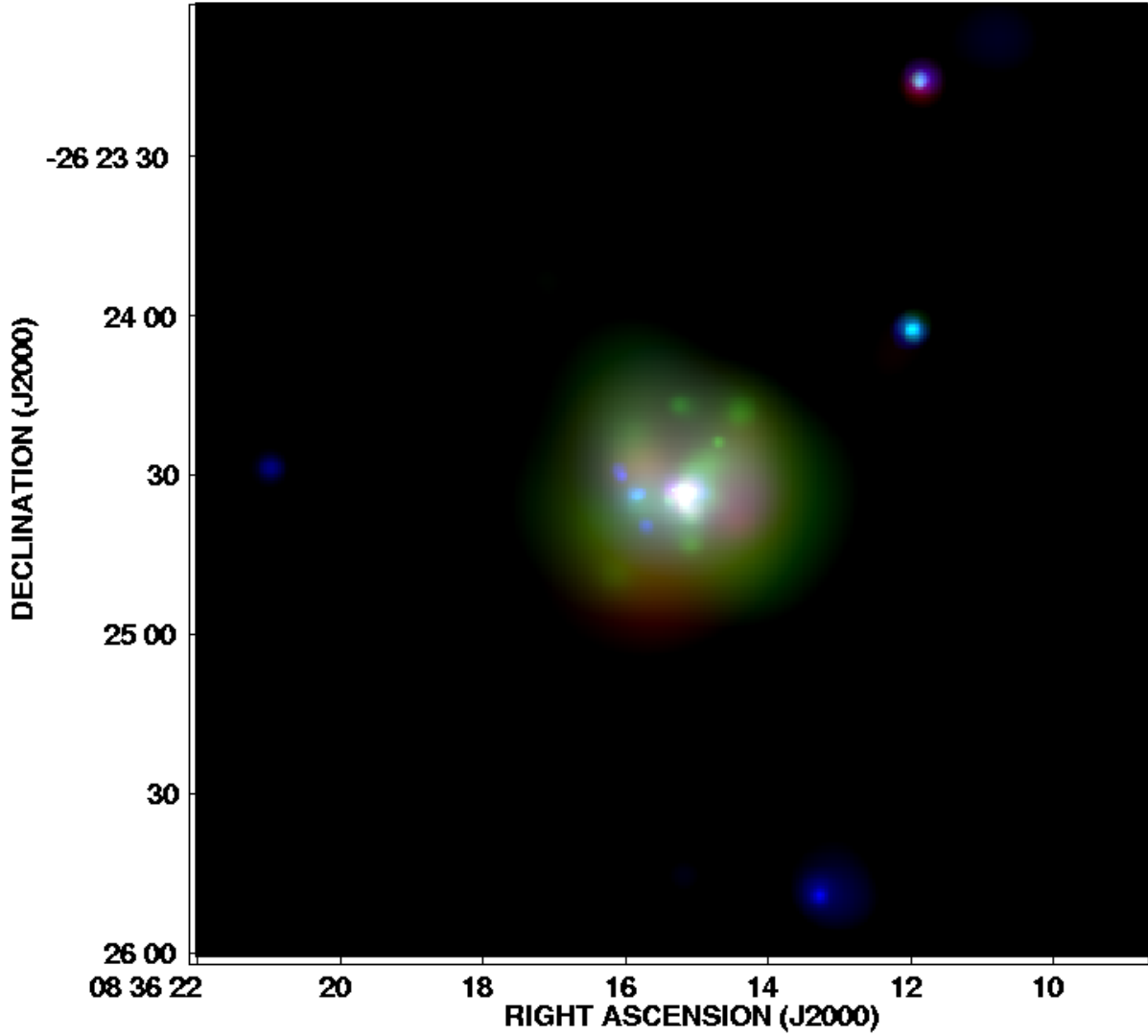


Fig. 8.— Composite 3-color X-ray image of Henize 2-10 with the soft 0.3–0.7 keV emission in red, the medium 0.7–1.1 keV emission in green, and the hard 1.1–6.0 keV emission in blue.

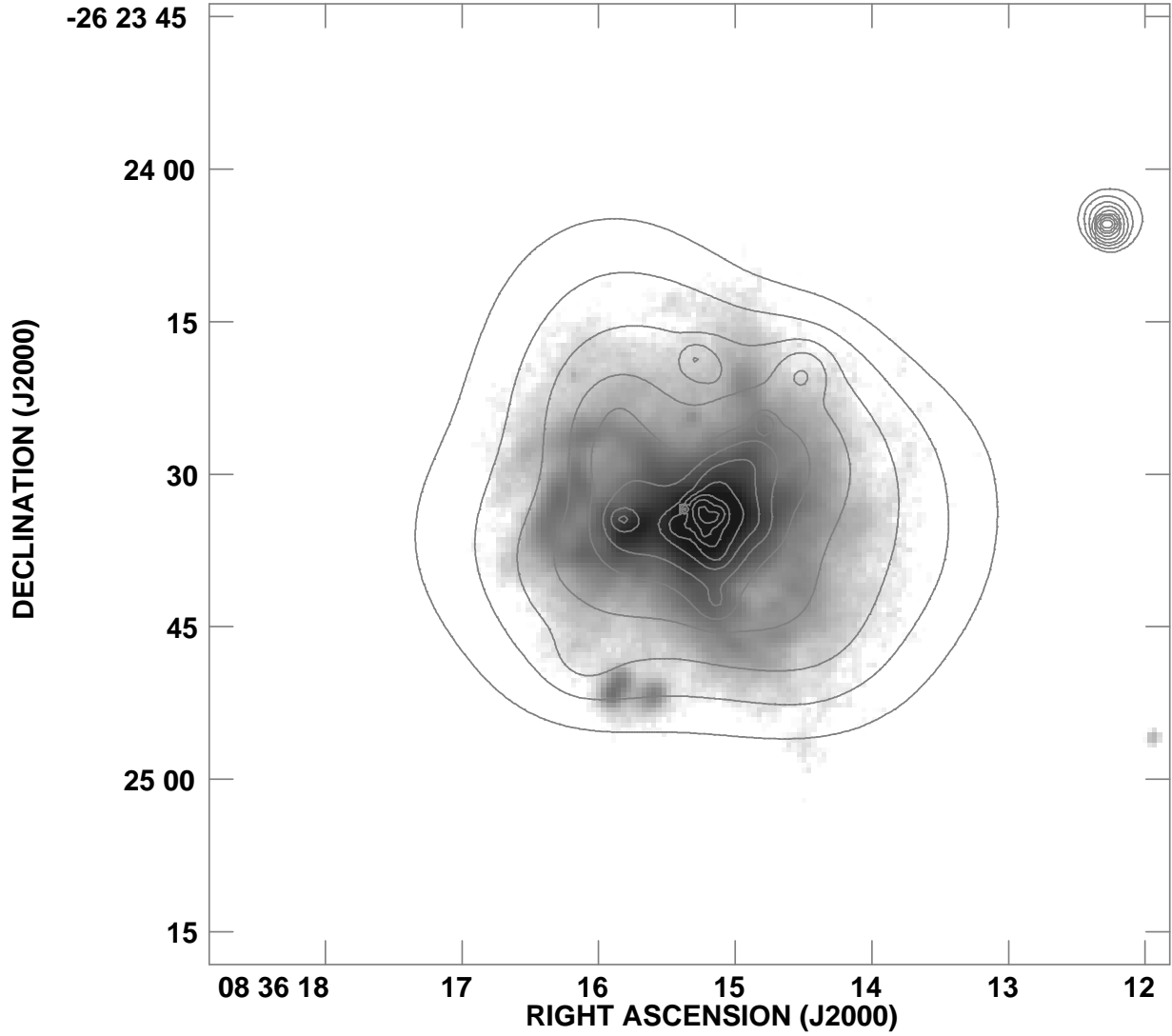


Fig. 9.— $H\alpha$ image of Henize 2-10 (grayscale) with medium band 0.7-1.1 keV X-rays in contours. Note the cone-shaped minimum to the north of the nucleus seen both in X-rays and in the warm ionized gas. $H\alpha$ shells extend to the east and southwest.

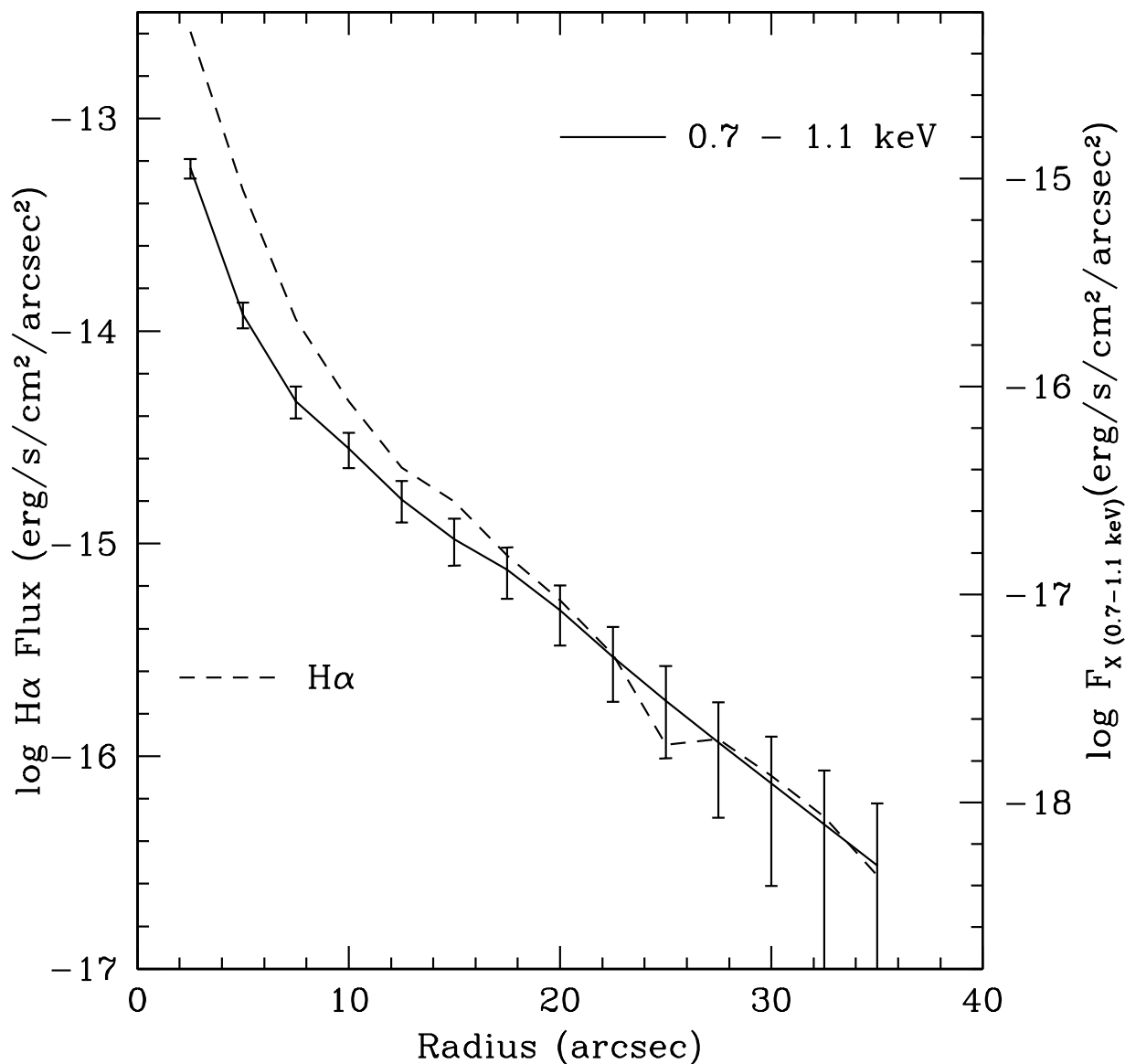


Fig. 10.— Azimuthally averaged radial profile of H α (solid line) and medium band X-ray (dotted line) surface brightness in Henize 2-10. The left abscissa shows the H α scale and the right abscissa shows the X-ray scale. The shape of the radial profiles in X-rays and H α are nearly identical except within $\sim 10''$ of the nucleus where extinction may be a significant factor.

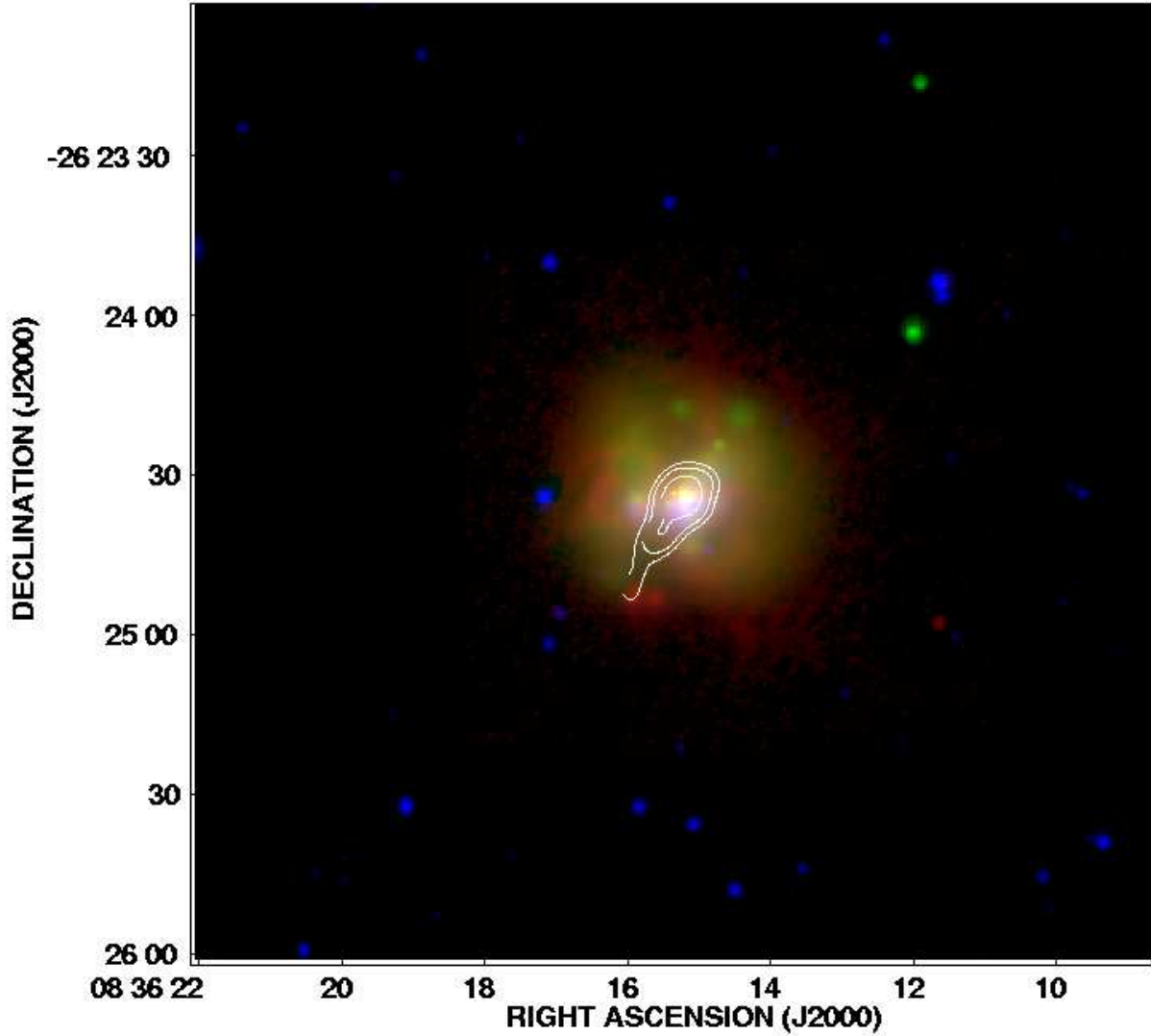


Fig. 11.— Composite three-color image of Henize 2-10 with the *Chandra* 0.7–1.1 keV emission in green, $H\alpha$ emission in red, and optical 6550 Å continuum image in blue. Contours show a putative disk of molecular gas as traced by ^{12}CO 1→0 emission from the Owens Valley Radio Interferometer mapped at a resolution of 5'' (Kobulnicky et al. 1995). $H\alpha$ shells extend to the E–NE and SW, perpendicular to the molecular extension.

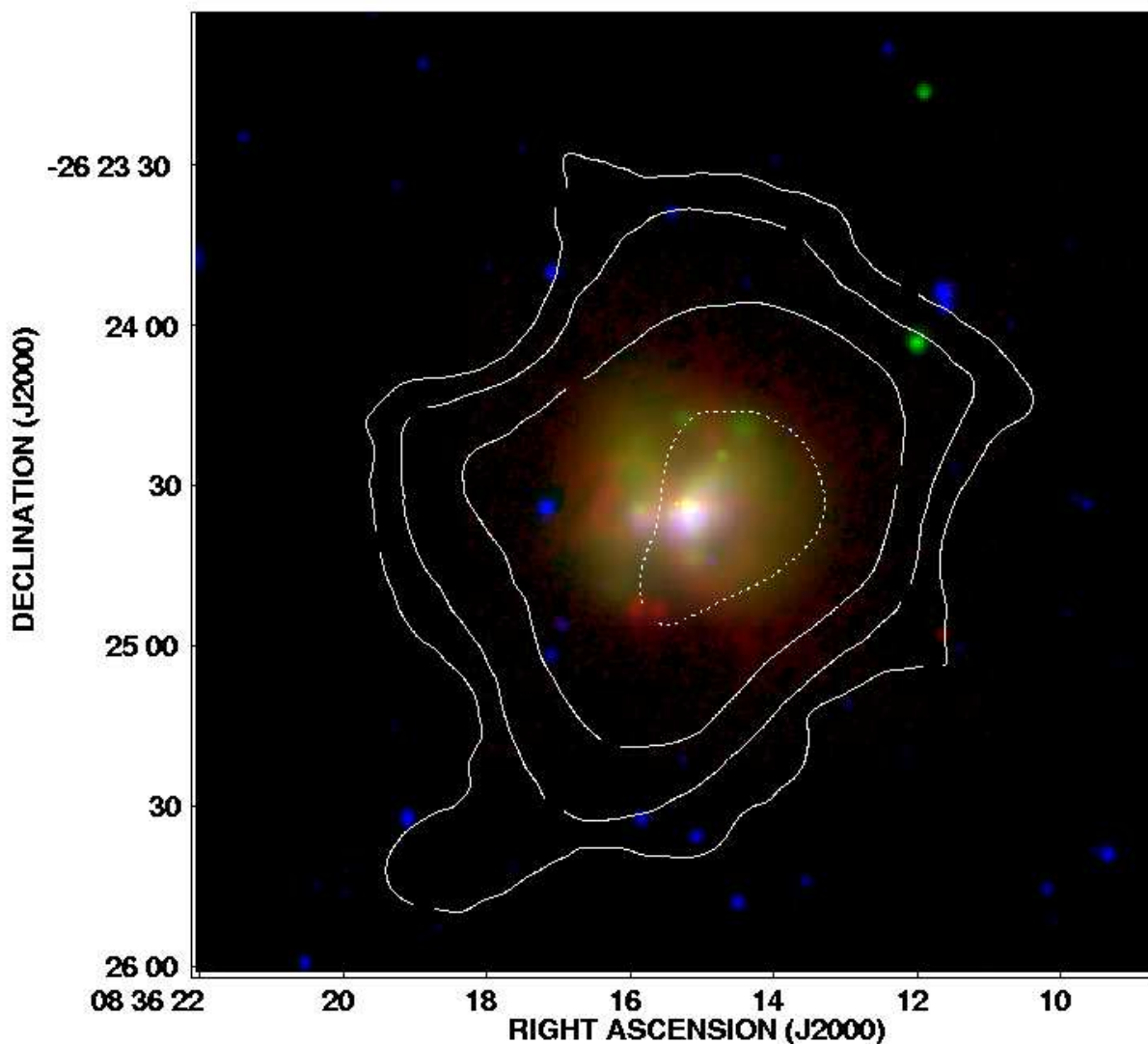


Fig. 12.— Composite three-color image of Henize 2-10 with the *Chandra* 0.7–1.1 keV emission in green, $H\alpha$ emission in red, and optical 6550 Å continuum image in blue. Contours show the neutral atomic gas as traced by H I 21-cm emission from the *VLA* mapped at a resolution of 30'' (Kobulnicky et al. 1995). Contours correspond to beam-averaged column densities of $N_{HI} = 2 \times 10^{20}$, 4×10^{20} , 8×10^{20} , and $16 \times 10^{20} \text{ cm}^{-2}$. Although the orientation of Henize 2-10 is uncertain, it appears that the full extent of X-ray and $H\alpha$ emission is contained within the neutral hydrogen envelope of the galaxy.

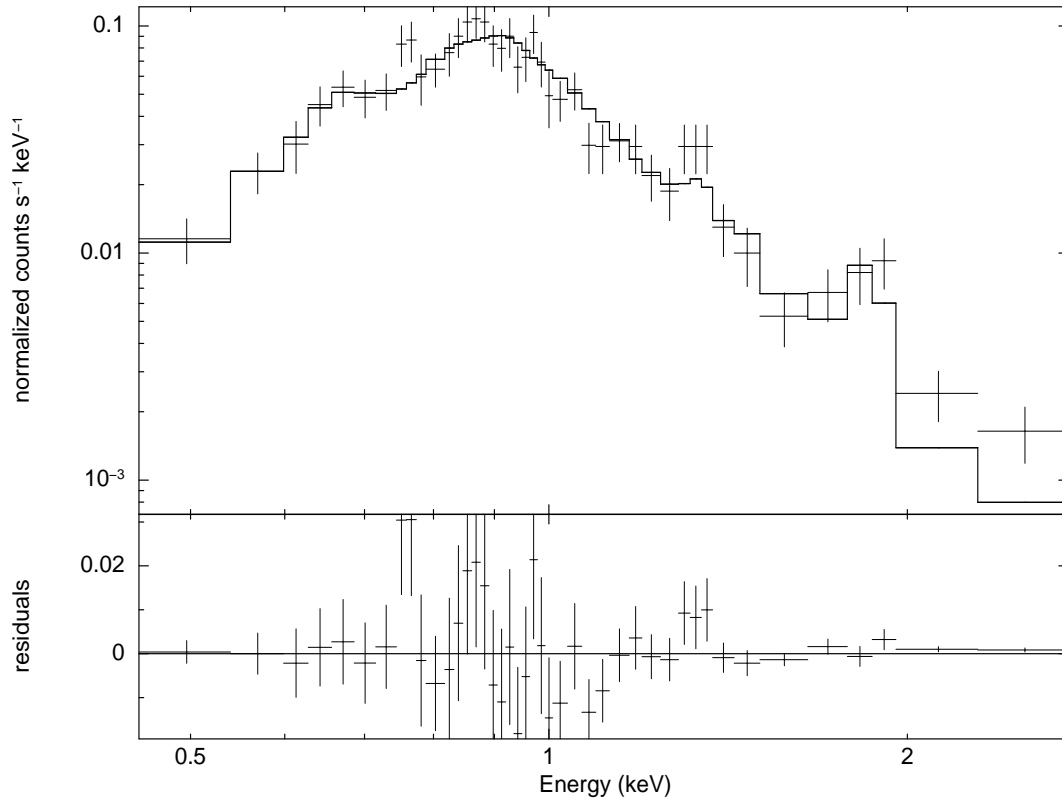


Fig. 13.— X-ray spectrum for the diffuse ISM in Henize 2-10 with the best fit two-component thermal plasma model (Model 1 of Table 4) and residuals.

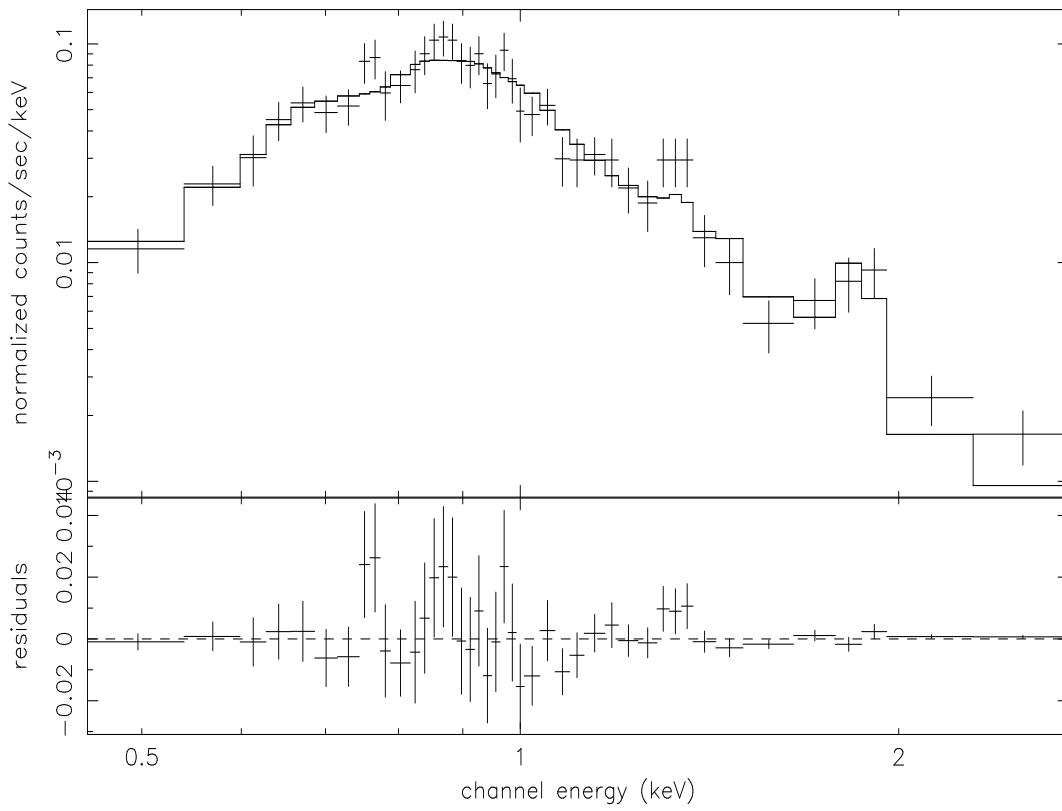


Fig. 14.— X-ray spectrum for the diffuse ISM in Henize 2-10 with the best fit single-component thermal plasma model with enhanced α/Fe ratios (Model 4 of Table 4) and residuals.